University of Tartu

Faculty of Science and Technology

Institute of Ecology and Earth Sciences

Department of Geology

Alvar Ratt

Pyrrhotite and pyrite trace element composition in Jõhvi magnetite quartzites, north-east Estonia: implications to sulphide mineralisation processes

Bachelor's thesis in Geology

Supervisors

Siim Nirgi

Kalle Kirsimäe

Kaitsmisele lubatud ……

Juhendaja ……

allkiri, kuupäev

Tartu 2022

Pyrrhotite and pyrite trace element composition in Jõhvi magnetite quartzites, north-east Estonia: implications to sulphide mineralisation processes

The aim of this thesis was to describe the origin of the pyrrhotite and pyrite mineralisation in the sulphide-magnetite and magnetite mineralisation intervals in the crystalline basement rocks sampled from the Jõhvi magnetic anomaly. Sulphide bearing samples from the sulphide mineralisation intervals of drill cores PA-1 and PA-2 were described petrographically, and the trace element composition of the sulphides was characterised by using analytical scanning electron microscopy and laser ablation inductively coupled plasma mass spectrometry. The results of this study show that sulphides are mainly of high temperature (250-300 °C) hydrothermal origin but also a population of the sedimentary sulphides is present. Some sulphides show very high cobalt content which is probably due to sub-micrometer scale Co-mineral inclusions.

Keywords: pyrite, pyrrhotite, trace elements

Pürrotiini ja püriidi jälgelementide sisaldus Jõhvi magnetkvartsiidis Kirde-Eestis: viited sulfiidi mineralisatsiooniprotsessidele

Käesoleva bakalaureusetöö eesmärk oli kirjeldada Jõhvi magnetilise anomaalia kristalsete aluskorrakivimites esineva sulfiidse maagistumise intervallides esinevate pürrotiini ja püriidi moodustumise tingimuse. Selleks võrreldi puursüdamike PA-1 ja PA-2 sulfiidse mineralisatsiooni intervallidest võetud proove petrograafiliselt, kirjeldati maakmineraalide esinemisvorme ning jälgelementide koostist skaneeriva elektronmikroskoopia ja laser-ablatsiooni induktiivsidestatud plasma massispektromeetria meetodil. Uuringu tulemused näitavad, et tekke poolest jagunevad sulfiidid valdavateks kõrgetemperatuurilisteks (250-300 °C) hüdrotermaalseteks ja settelisteks sulfiidideks. Mõnedes intervallides iseloomustab uuritud sulfiide (peamiselt püriit) eriti kõrge koobalti sisaldus. Sellise rikastumise põhjused ei ole täiesti selged kuid on arvatavasti seotud Co-mineraalide mikrosuletistega püriidis.

Märksõnad: püriit, pürrotiin, jälgelemendid

Table of contents

Introduction

Estonian crystalline basement exhibits several strong magnetic anomalies possibly caused by magnetite rich rock units (Figure 1). The strongest is the Jõhvi Magnetic Anomaly (JMA, up to 19,300 nT, Plado et al., 2020) which was already discovered in early 1930s. Detail geophysical mapping and the first drilling campaign of the anomaly was undertaken between 1935–1939 resulting in two deep drill holes (Jõhvi-I and Jõhvi-II) that intersected magnetite quartzite rocks in the crystalline basement (Linari, 1940). The geological exploration of JMA continued in the 1960s when additional geophysical mapping (gravimetric and magnetometric) of the area was performed in 1961 and 1964–1965, and additional drilling was made in 1967-1968 (Suuroja, 1969; Erisalu & Arvisto, 1969; Nirgi et al., 2022).

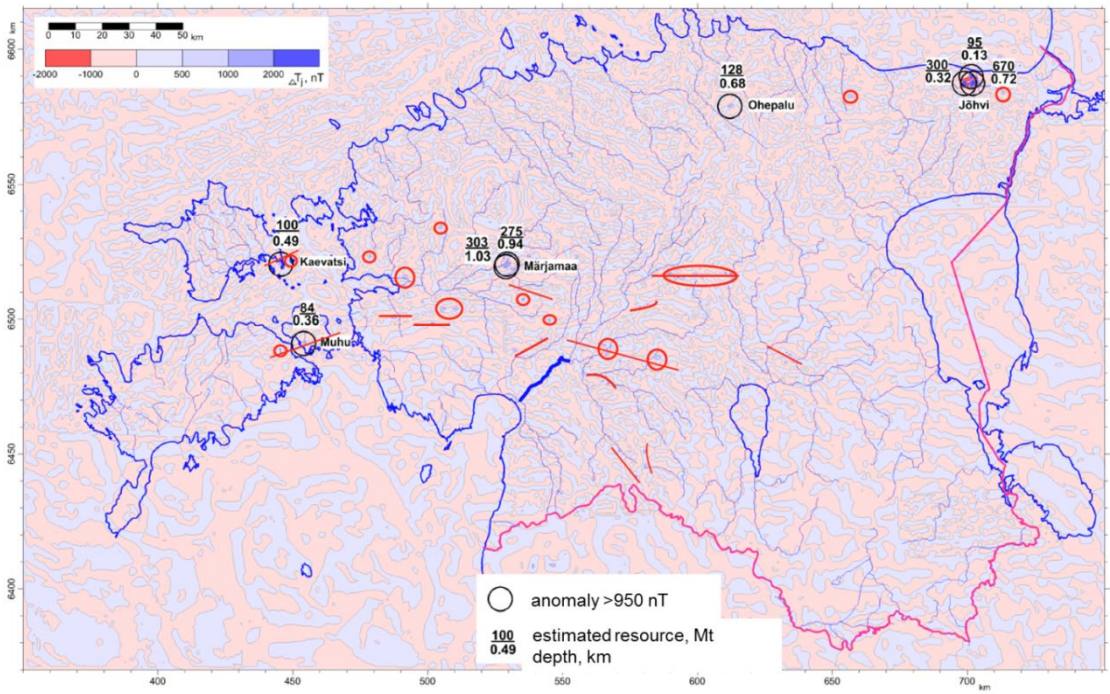

Figure 1. Map of the residual anomalies of the magnetic field of Estonian territory with the main magnetic anomalies and their potential magnetite resource and the estimated depth of the rock body centre. Compiled by M. Shtokalenko, Estonian Geological Survey (2021).

The investigation of the JMA was continued again in 2019 when Geological Survey of Estonia drilled in the Jõhvi Magnetic Anomaly area two 770 m deep inclined diamond core boreholes. The new drilling was undertaken to estimate the exploration potential of the iron mineralisation and to investigate the presence of other mineralisation types (Nirgi et al., 2022). The studies of the new cores confirmed the main results of the earlier studies showing that the Jõhvi Magnetite

Anomaly is caused by sub-vertical, partially mineralised metamorphic rocks rich in magnetite of the crystalline basement below the sedimentary cover at the depth of 240 m extending possibly to the depth of 1000 m.

In addition to magnetite quartzites and magnetite-rich gneisses, sulphide and magnetite-sulphide mineralised intervals occurs. Sulphide mineralisation is predominantly represented by pyrrhotite and in a lesser extent by pyrite and chalcopyrite. The sulphide mineralisation was noted already during the earlier investigations of the JMA magnetite quartzite and Cu (up to 0.7 wt% according Luha, 1946) and Zn 0.42% were reported, respectively (Linari, 1940). However, no specific study has been conducted for associated Cu-Zn/Pb mineralisation in JMA. Interestingly, rare As-minerals arsenopyrite and löllingite were identified during the core logging of the latest drill cores PA-1 and PA-2 (Nirgi et al., 2022). These finds with the first discovery of the native visible Te, Bi, Ag and Au in JMA mineralised zones (K. Kirsimäe, unpublished data, 2022) open new perspectives for metal exploration in the Estonian crystalline basement.

In this thesis, the trace element composition of the sulphide phases in sulphide and magnetite-sulphide mineralisation occurrences from the new Jõhvi drill cores PA-1 and PA-2 are analysed and discussed. Trace elements taken up during the crystallisation of the main sulphides are useful for understanding the mineralisation processes, origin and composition of the mineralising hydrothermal fluids (Large et al., 2009; Duran et al., 2015; Cook et al., 2016; Keith et al., 2018). It is also important that several trace elements occurring in pyrite and pyrrhotite can be used as pathfinders for precious and base metal ores.

The aim of this thesis is to decipher the conditions during the sulphide mineralisation in crystalline basement rocks of the Jõhvi Magnetic Anomaly.

Geological Setting

The Paleo- to Meso-Proterozoic Precambrian crystalline basement of Estonia consists of the orogenic Svecofennian metamorphic and plutonic rocks, and the anorogenic plutonic rapakivi granites intersecting the Svecofennian metamorphic complex (Puura et al., 1996, Figure 2). Peneplaned and weathered surface of the crystalline basement dips 2 to 4 m/km to the south being covered by *ca*. 100 m (in northern Estonia) to *ca*. 800 m thick (in southern and south-western Estonia) sequence of Neoproterozoic and Palaeozoic sedimentary succession. Thus, there are no outcrops of crystalline basement in the Estonian area. Structurally the crystalline basement of Estonia is considered to be similar to the Svecofennian Domain of the Fennoscandian Shield (Bogdanova et al., 2015) and it is composed of two major units - amphibolite facies metamorphic rocks dominate in northern Estonia, and metamorphic rocks reaching the granulite facies in southern Estonia (Puura et al., 1996; Soesoo et al., 2004).

These metamorphic zones are subdivided into six zones based on their petrological and geophysical characteristics: the Tallinn, Alutaguse, Tapa, West Estonian, South Estonian and Jõhvi Zones (Figure 2; Puura et al., 1996; Soesoo et al., 2004).

According to Puura et al. (1996) and Soesoo et al. (2004, 2020) the Tallinn Zone is characterised by metavolcanic and metasediments (amphibole gneisses, biotite-plagioclase gneisses, quartz-feldspar gneisses, mica gneisses, and sulphide-graphite gneisses and magnetite quartzites) of the amphibolite facies rocks. The Alutaguse Zone is characterised mainly by metasedimentary Al-rich gneisses and biotite-plagioclase gneisses, and some amphibole gneisses, amphibolites and quartz-feldspar gneisses of the amphibolite facies. The Tapa Zone is characterised by garnet and pyroxene quartzites, Al (garnet-cordierite-sillimanite) gneisses, and pyroxene-, amphibole- and biotite gneisses rich in Fe and S whereas the metamorphic grade varies between amphibolite and granulite facies. The West-Estonian Zone is characterised by mainly metasedimentary amphibolites, biotite-plagioclase gneisses, and quartz-feldspar gneisses of amphibolite to granulite facies. The South-Estonian Zone is characterised mainly by metavolcanic metamorphic rocks that have underwent the granulitic facies metamorphism where the main rock types are amphibole-pyroxene and biotite-pyroxene gneisses with quartz-feldspar gneisses.

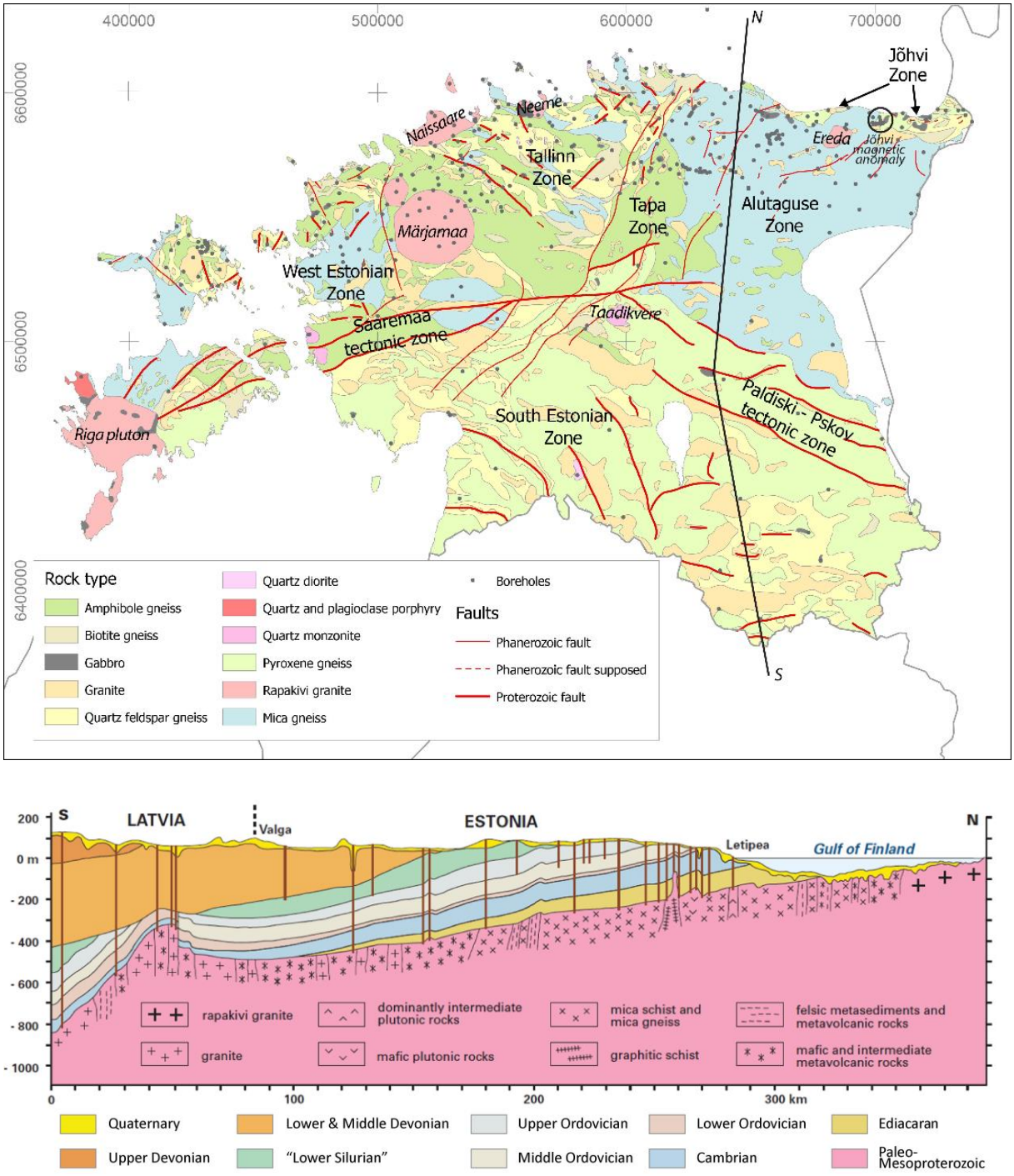

Figure 2. Geological map of the Estonian crystalline basement and cross-section of the sedimentary cover and crystalline basement along the N-S (Modified after Vaher et al., 1962; Estonian Geological Survey)

Jõhvi Zone where the Jõhvi Magnetic Anomaly occurs, forms a narrow 20 to 30 km wide and 100 km long belt (Figure 2) within the amphibolite grade gneisses of the Alutaguse Zone north-east Estonia. Crystalline rocks in Jõhvi Zone are characterised by migmatised gneisses/granites of different compositions (Figure 3). The main rock types are pyroxene gneisses, quartz-

feldspar gneisses, biotite-plagioclase gneisses, amphibole gneisses, garnet-cordierite gneisses that are collectively known as Vaivara complex and the Jõhvi magnetite-rich gneisses/quartzites (Figure 3; Soesoo et al., 2020; Nirgi et al., 2022). The rocks have been to granulite facies metamorphism and the bedding of gneisses and magnetite bearing quartzites is subvertical (Soesoo et al., 2020; Nirgi et al., 2021).

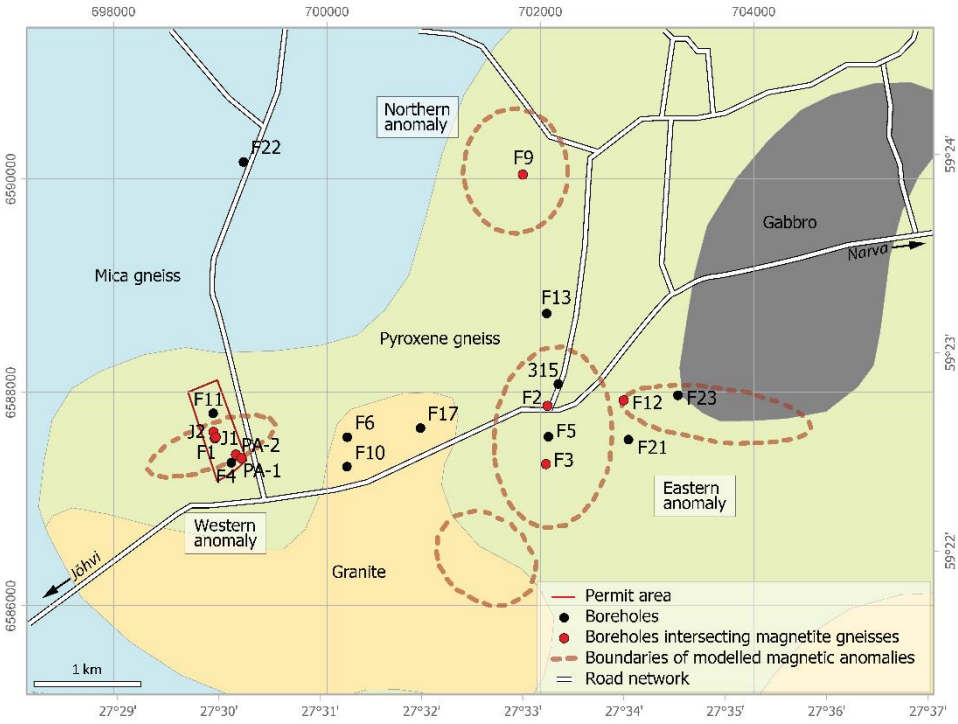

Figure 3. Geological map of the crystalline basement of the Jõhvi Magnetic Anomaly with location of boreholes (including drill cores PA-1 and PA-2 studied in this thesis) and boundaries of modelled sources of magnetic anomaly (from Nirgi et al., 2022; after Koppelmaa, 2002 and Plado et al., 2020)

The Jõhvi magnetite-rich gneisses/quartzites occur as subvertical beds in garnet-cordierite or pyroxene gneisses whereas the whole rock successions in both cores are intersected by numerous migmatite granites that show variable apparent thicknesses up to 34.6 m (Nirgi et al., 2022).

The magnetite rich rocks cause the magnetic anomaly that is characterised by several magnetic anomaly maxima reaching up to 19 300 nT in the so-called western anomaly (Figures 3 and 4) accompanied with slight positive gravity anomalies (Plado et al., 2020). The mineralised zones in JMA rocks are represented by predominant magnetite and/or magnetite-sulphide mineralisation and in drill cores PA-1 and PA-2 the total apparent thickness of the mineralised

intervals is more than 100 m (Nirgi et al., 2022). The thickness of separate magnetite rich mineralisation intervals varies between 0.12 to 50.0 m while the individual interval magnetite-sulphide mineralisation zones range from 0.20 to 30.85 m in thickness (Nirgi et al., 2022).

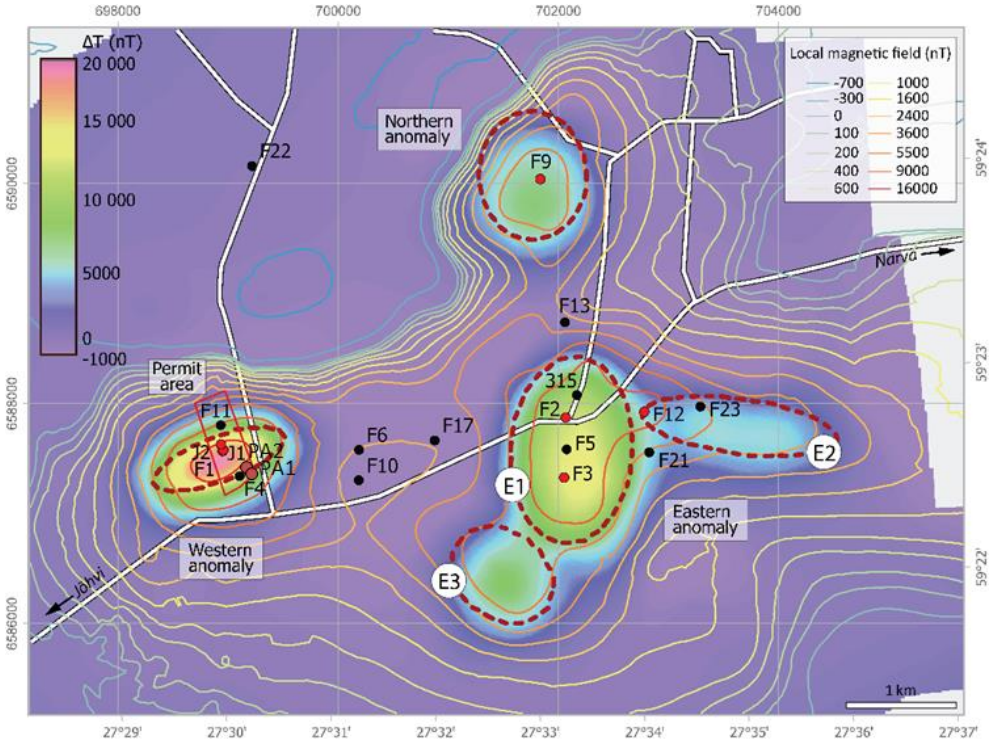

Figure 4. The Jõhvi Magnetic Anomaly on total magnetic intensity anomaly map with indication of the surface projection of the potential orebodies (red dashed lines). The red dots show historical borehole locations where magnetite-rich gneiss was intersected. Coordinates are in the Estonian Coordinate System of 1997 (L-EST97; EPSG:3301) (from Nirgi et al., 2022, modified after Plado et al., 2020).

Trace elements in pyrite and pyrrhotite

During the formation of Fe-sulphides, a wide variety of elements in trace to minor amounts (sub-ppm to first weight % levels) are incorporated, either by substitution into the crystal lattice or as nano- to micro-scale inclusions of other minerals; the most common are Co, Ni, As, Se, Zn, Cu, Au, Ag, Te, Pb, Sb, Bi, Tl, V, Mn, PGEs, and Hg (Cook and Chryssoulis, 1990; Reich et al., 2013; Large et al., 2009; Steadman et al., 2015, 2021; Sykora et al., 2018; Mathieu, 2019).

Elements like As, Co, Ni and Se typically substitute for either Fe or S (or both) whereas As can be also present as arsenopyrite nanoparticles when the As concentrations are higher than 5 wt%. Though Cu, Zn, Te, Pb, Bi, Ag and Au can substitute into the crystal structure then these elements occur more commonly as nanoparticles and micro-inclusions of Cu-Pb-Ag sulphides or sulphosalts, native Au or electrum (Ag-Au), and Au-Ag/Bi/Pb tellurides forming in fracture zones of sulphide grains (Steadman et al., 2021). Mn, V, Tl, Hg and also W are typically substituting into the crystal structure at lower temperatures processes in epithermal or VHMS-type (volcanic-hosted massive sulphide) sulphides (Deditius and Reich, 2016).

It is important that Fe-sulphide trace-element composition reflects the environmental conditions during its formation – the pyrites in high-temperature hydrothermal systems are characterised by elevated concentrations of Ni, Co, Se and Te and Se (Steadman et al., 2021). Steadman et al. (2021) and Maslennikov et al. (2009) have proposed that sulphides can be grouped by their trace element characteristics into four temperature zones:

1. high-temperature group (>300 °C) – typified by elevated Co, Ni, Cu, Se, Te and Bi;
2. mid-temperature group (200–300 °C) – Zn, As, Sb, and Sn;
3. low-temperature group (150–200 °C) – Pb, Sb, Ag, Bi, Au, Tl and Mn;
4. seawater/diagenetic group – U, V, Mo, and Ni.

Maslennikov et al. (2009) points out that the trace elements in the high-mid temperature associations can be also incorporated under low-temperature but the trace elements in groups 3 and 4 can only precipitate at low-temperatures because their solubility is high in reduced high- and mid-temperature fluids which makes Se/Tl in hydrothermal pyrite a robust proxy for temperature. It is also typical that at lower temperatures the disorder in the rapidly forming crystal structures causes non-stoichiometric elemental substitutions allowing incorporation of elements with large ionic radii like Tl, Sb, and Hg whereas at higher fluid temperatures the

high diffusion rates and slower growth rates leads to more ordered crystal structures that does not allow the incorporation of such elements (Steadman et al., 2021). Besides of temperature the incorporation of trace elements in sulphides is influenced by pH, salinity, oxygen and sulphur fugacity, and the redox state of the forming fluid (Steadman et al. (2021).

Material and Methods

Altogether 15 samples were collected from drill cores PA-1 and PA-2 intersecting magnetite and sulphide mineralisation zones (Figure 5). Samples were collected from separate mineralised zones and intervals of different mineralisation morphology (e.g., disseminated, massive, vein) in order to study the spatial variability of iron sulphides and the characteristics of variable forms of iron sulphides. 13 slabs were cut and polished from sulphide bearing drill-core samples and two thin sections from the archive of the geological survey were used.

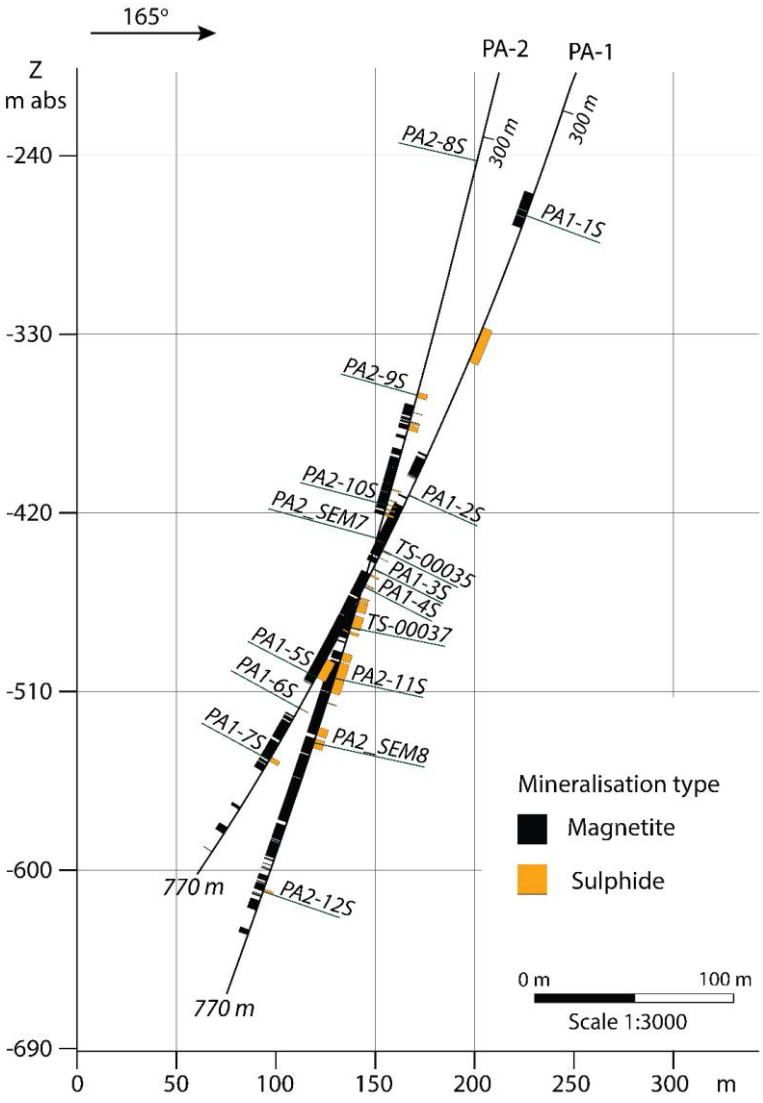

Figure 5. Schematic drill hole profiles of PA-1 and PA-2 with mineralised intervals and locations of collected samples.

Slabs and thin sections were inspected under the binocular and optical polarizing microscope in transmitted and reflected light, and in scanning electronical microscope using back-scattered

electron (BSE) imaging with ZEISS EVO MA15 SEM equipped with Oxford AZTEC-MAX energy-dispersive (EDS) system.

Trace element concentration measurements were performed with laser ablation inductively coupled plasma mass spectrometry (LA-ICP-MS) using an Agilent 8800 quadrupole ICP-MS coupled to a Cetac LSX- 213 G2+ laser with HelEx II fast-washout two-volume large-format cell and 'Squid' smoothing interface at University of Tartu. Spot analysis on the samples was performed using the following laser parameters: fluence 3.2J/cm^2, repetition rate 10 Hz, 50 µm round spot. 20s of gas blank were collected before each ablation pass and ablation signal was collected for 45s. USGS GSD1G and MASS1 were used as the calibration standard and were measured in triplicates after 20 sample ablations. The oxide formation ratio expressed as ThO/Th from ablation of NIST 610 during instrument tuning was <0.25%.

Signals of ^{27}Al, ^{29}Si, ^{34}S, ^{43}Ca, ^{44}Ti, ^{51}V, ^{53}Cr, ^{55}Mn, ^{57}Fe, ^{59}Co, ^{60}Ni, ^{66}Zn, ^{95}Mo, ^{107}Ag, ^{118}Sn, ^{121}Sb, ^{182}W were collected with a dwell time of 6 ms, ^{63}Cu, ^{75}As, ^{77}Se, ^{209}Bi with a dwell time of 10ms and ^{125}Te, ^{197}Au, ^{201}Hg, ^{205}Tl and ^{208}Pb were collected with a dwell time of 20 ms, surmounting to a total duty cycle of 0.33s on the ICP-MS.

Data reduction of the raw signals were performed using Iolite V3.62. After background substitution X_Trace_Elements IS data reduction scheme with quantitative standardisation method using Fe as an internal standard element was used for concentration calculations. For ^{34}S, ^{53}Cr, ^{77}Se, ^{125}Te and ^{201}Hg MASS1 was used as the calibration standard and for all other elements GSD1G. For samples, a stoichiometric Fe concentration based on the ablated mineral was assumed as 46.55% Fe in pyrite and 62.33% Fe in pyrrhotite.

Because of numerous silicate and other mineral impurities/inclusions, the LA-ICP-MS raw data were filtered and the data where Si, Ca or Al content was over 500 ppm were excluded from further analysis. Altogether 246 laser spots were used in the data analyses of which 146 are pyrite and 103 pyrrhotite.

Results

Sample Petrography

Sulphide mineralisation in JMA drill cores PA-1 and PA-2 is characterised by dominant pyrrhotite and/or pyrite with minor chalcopyrite and rarely arsenopyrite and löllingite with microscopic occurrences of sphalerite, galenite and Pb-Bi(Te)-Ag sulphosalts. The main sulphides are either scattered throughout the magnetite-rich rocks or massive aggregates with magnetite and in some cases as thin (mm-scale) sulphidic veins.

Sample PA1-1s (PA-1; 359.70–359.75 m) is from K-feldspar-quartz vein in pyroxene-garnet-amphibole-magnetite-quartz gneiss where pyrite together with chalcopyrite occurs as irregular mm-size patches filling the space between brecciated K-feldspar and quartz aggregate (Figure 6A).

Sample PA1-2s (PA-1; 527.70–527.75 m) is from pyrite bearing garnet-quartz-feldspar vein where up to a few cm size pyrite and pyrrhotite patches and veins occur in deformed and fractured host-rock (Figure 6B). Some of the macroscopic pyrite crystals show euhedral (cubic) crystal faces.

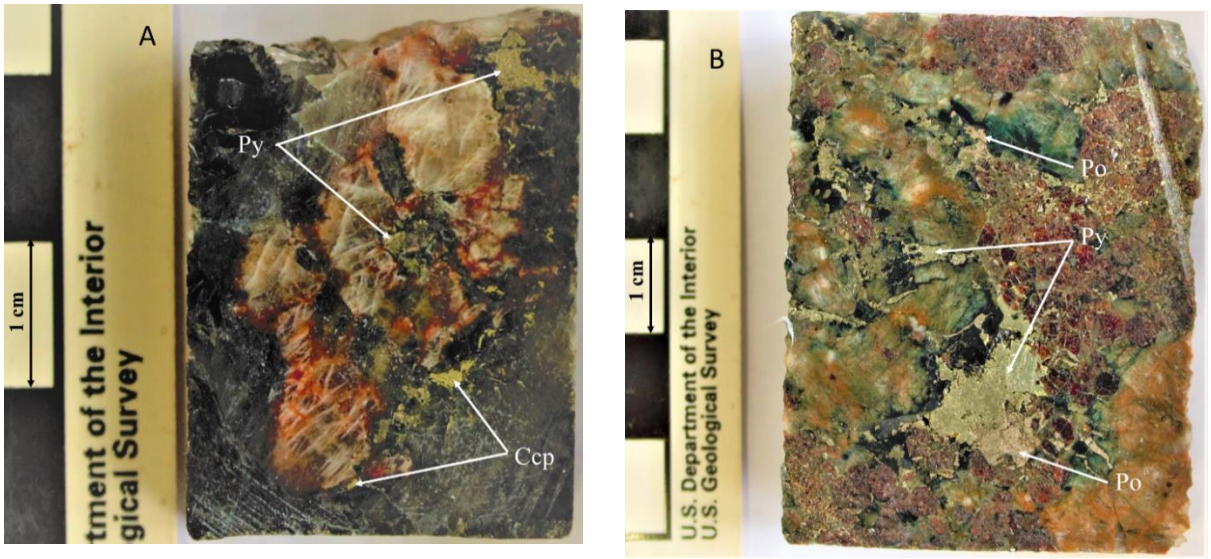

Figure 6. Optical images of Pyrite (Py) and Chalcopyrite (Ccp) mineralisation in brecciated K-feldspar-quartz vein. Sample PA1-1s (A), depth 359.70–359.75 m; and Pyrite (Py) and Pyrrhotite (Po) mineralisation in fractured garnet-quartz-feldspar vein. Sample PA1-2s (B), depth 527.70–527.75 m.

Under scanning electron microscope (Figure 7) the pyrrhotite appears as a massive aggregate with numerous sub-micron chlorite and K-mica inclusions. The pyrite crystals, however, are commonly fractured and the veins are filled with quartz, chlorite and garnet.

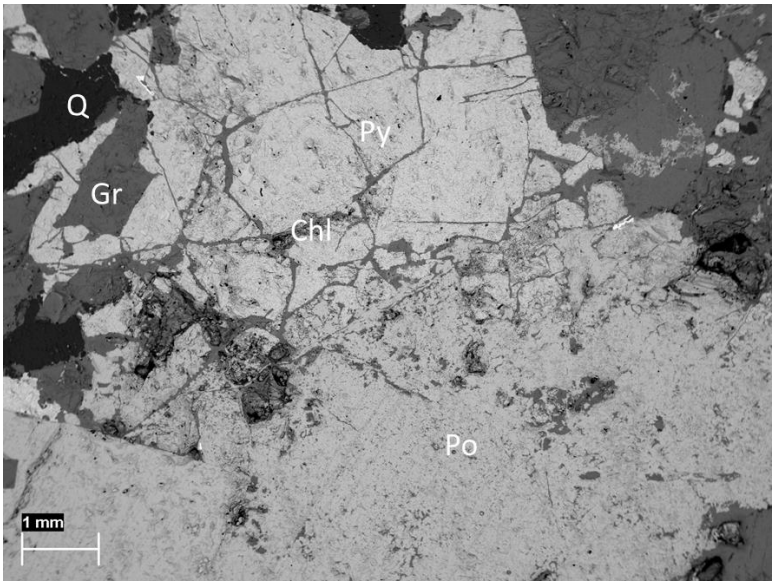

Figure 7. Backscattered scanning electron microscope image of the pyrite (Py) and pyrrhotite (Po) mineralisation in brecciated garnet-quartz-feldspar vein. Gr – garnet, Q - quartz, Chl - chlorite. PA-1 drill core, depth 527.70–527.75 m.

Sample TS-00035 (PA-1; 562.00–562.05 m) is from pyrrhotite bearing magnetite-garnet-amphibole-plagioclase-quartz gneisses occur. The pyrrhotite that is in places massive fills the space in the fractured host rock that is also cut with quartz filled veinlets (Figure 8).

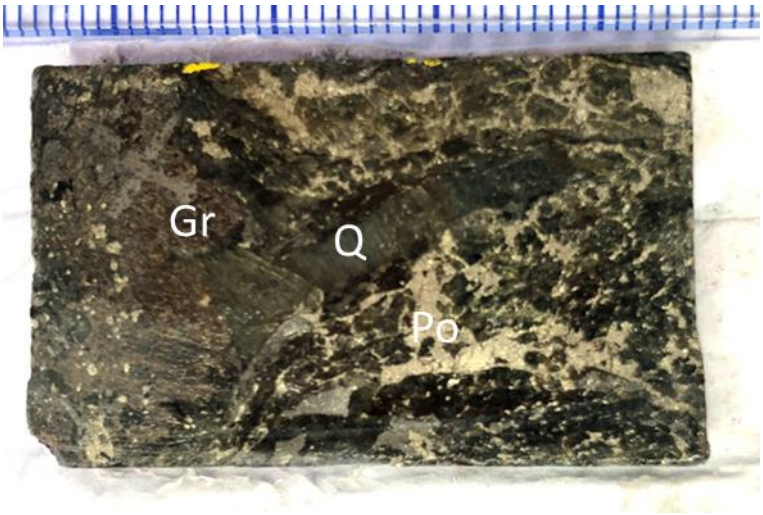

Figure 8. Pyrrhotite (Po) mineralisation in brecciated magnetite bearing rocks in drill core PA-1, depth 562.00–562.05 m.

In scanning electron microscope images (Figure 9) the pyrrhotite in sample TS-00035 forms anhedral masses intruding the deformed samples filling cracks in pre-existing minerals.

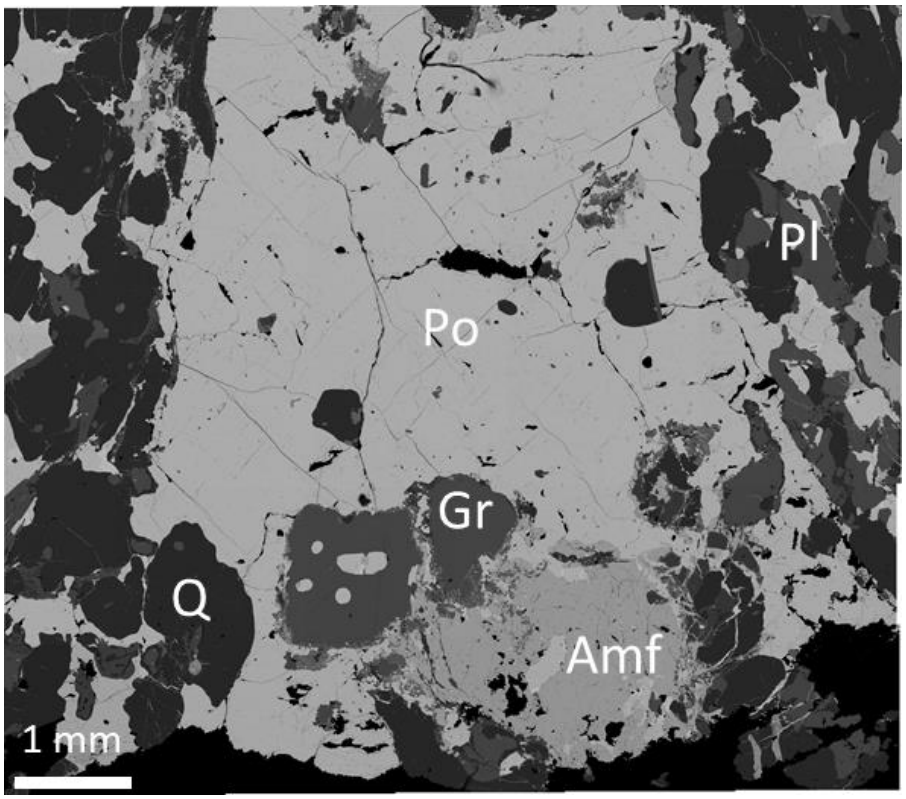

Figure 9. Backscattered scanning electron microscope image of the pyrrhotite (Po) mineralisation in brecciated garnet-amphibole quartz-feldspar gneisses. Gr – garnet, Q - quartz, Pl – plagioclase, Amf - amphibole. PA-1 drill core, depth 562.00–562.05 m.

Sample PA1-3s (PA-1; 573.45–574.50 m) (Figure 10A) is from pyrite bearing garnet-biotite-quartz-feldspar gneiss. The pyrite and pyrrhotite occurs as coarse-grained euhedral-subhedral aggregates in deformed and brecciated host rocks and the largest size of the crystallites reaches *ca*. 0.5–1.0 cm.

Sample PA1-4s (PA-1; 584.50–584.55 m) (Figure 10B) represents pyrrhotite diffuse bands. The host rock is pyroxene-garnet-quartz-magnetite gneiss. The pyrrhotite in up to 1 cm wide bands occurs as sub-mm size scattered anhedral crystallites. The orientation of the bands follows the direction of the magnetite banding.

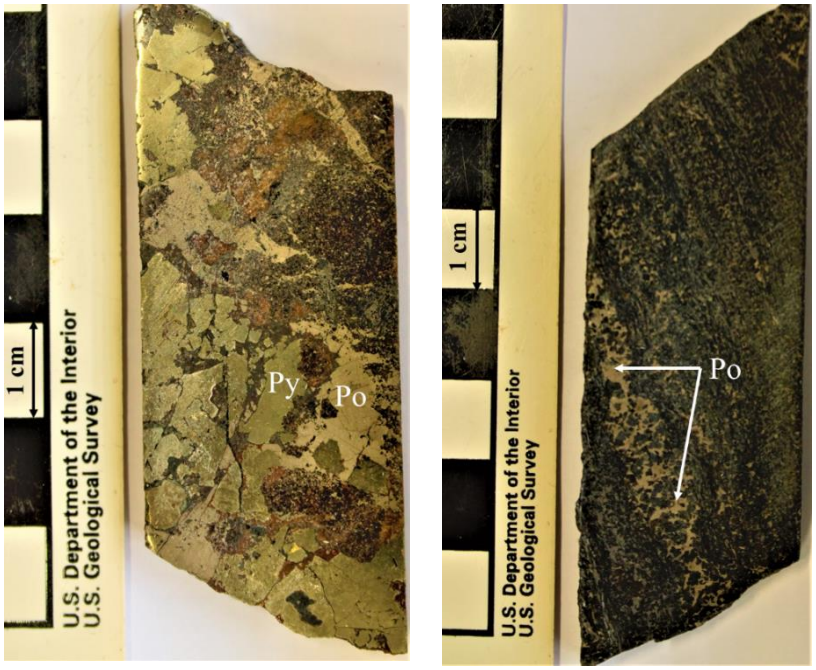

Figure 10. Optical images of pyrrhotite (Po) and pyrite (Py) mineralisation samples PA1-3s (A), PA-1 depth: 573.45–574.50 m; and PA1-4s (B), PA-1 depth 584.50–584.55 m.

Sample PA1-5s (PA-1; 641.30–641.35 m) (Figure 11) is from pyrite-garnet-quartz-magnetite gneiss host rock where thin mm-scale pyrite vein crosscuts the rock at about 20-30° angle respective to the magnetite-bearing gneiss banding. Pyrite is found also scattered through the magnetite bearing gneiss all over the surface of the sample. In scanning electron microscope, the pyrite does not form a vein with clear walls to the host rock but occurs rather as micrometre scale euhedral crystallites forming a diffuse up to 1-mm wide zone crosscutting the magnetite-quartz banding (Figure 12 A, B).

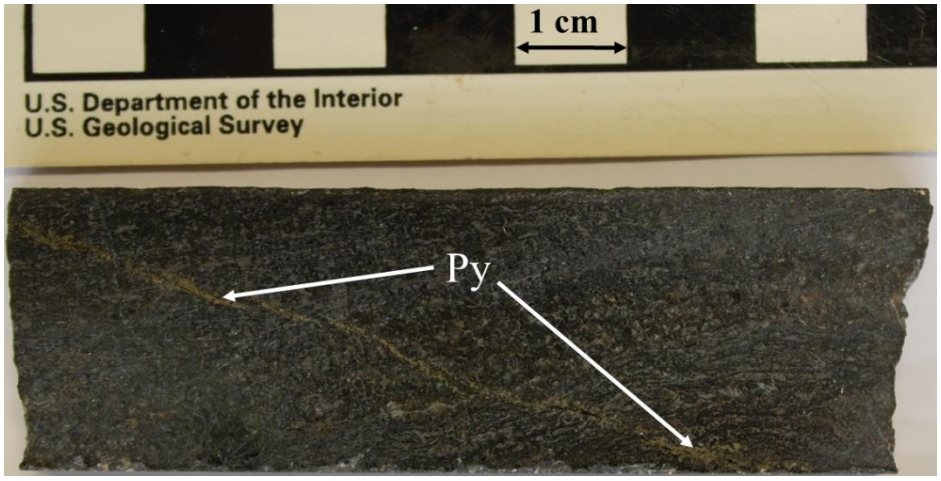

Figure 11. Optical image of the sample PA1-5s, PA-1 depth 641.3–641.35 m bearing a thin pyrite vein (Py).

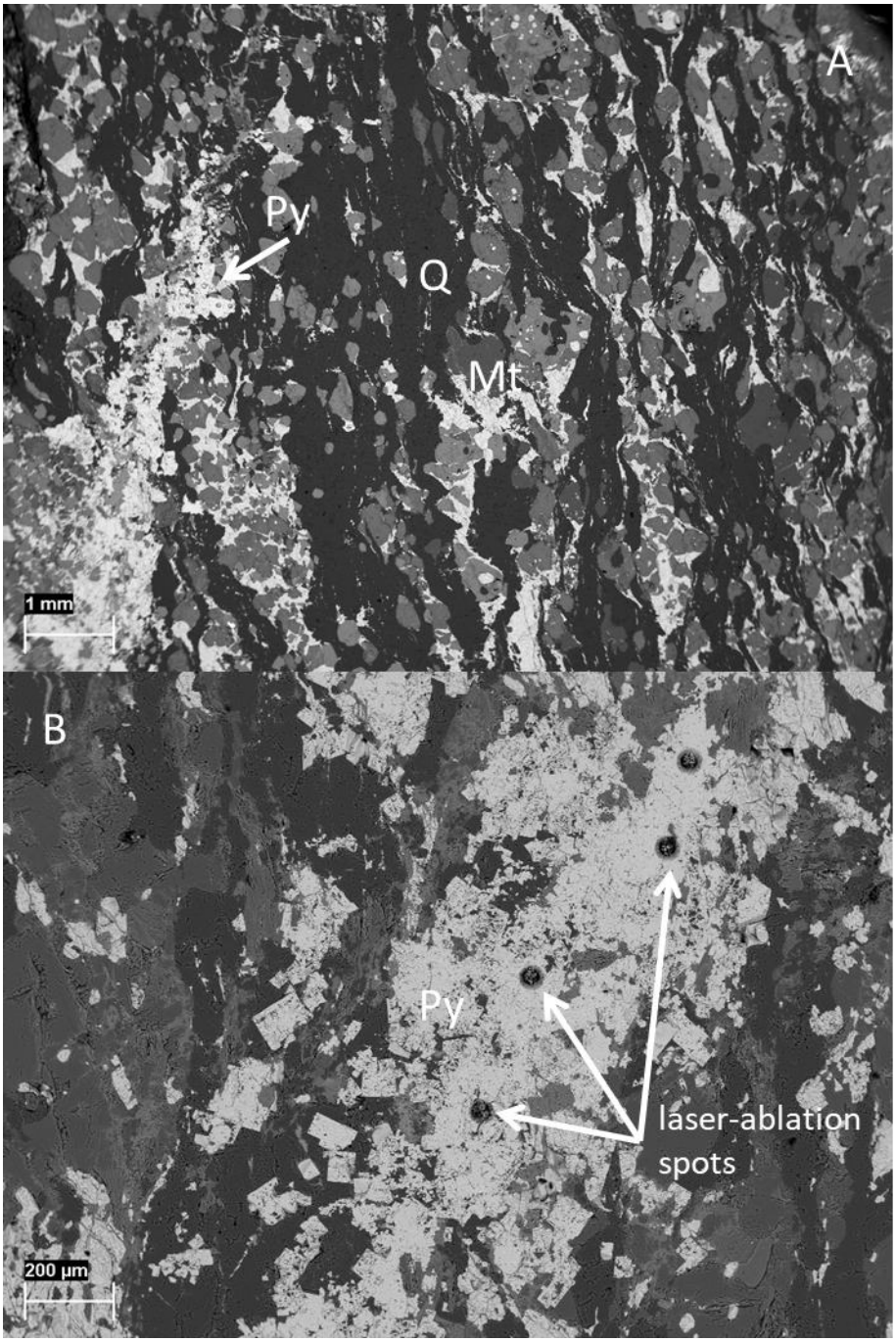

Figure 12. Backscattered scanning electron microscope image of the pyrite (Py) vein in magnetite bearing-gneiss of the sample PA1-5s, PA-1 depth 641.3–641.35 m. Q - quartz, Mt - magnetite. A - general view, B – close up of the area indicated with an arrow in A.

Sample PA1-6s (PA-1**;** 661.00–661.05 m) (Figure 13) is taken from the interval where pyrite bearing garnet-quartz-biotite-feldspar gneisses occur. The rock is heavily fractured and cut by pyrite and quartz veins. Also, minor chalcopyrite is found in this interval. In scanning electron microscope images, the pyrite occurs as subhedral to euhedral crystal aggregates with frequently cubic and octahedral crystal outlines (Figure 14). The chalcopyrite occurs either as

numerous sub-microscopic inclusions in pyrite or as small anhedral masses together with euhedral pyrite.

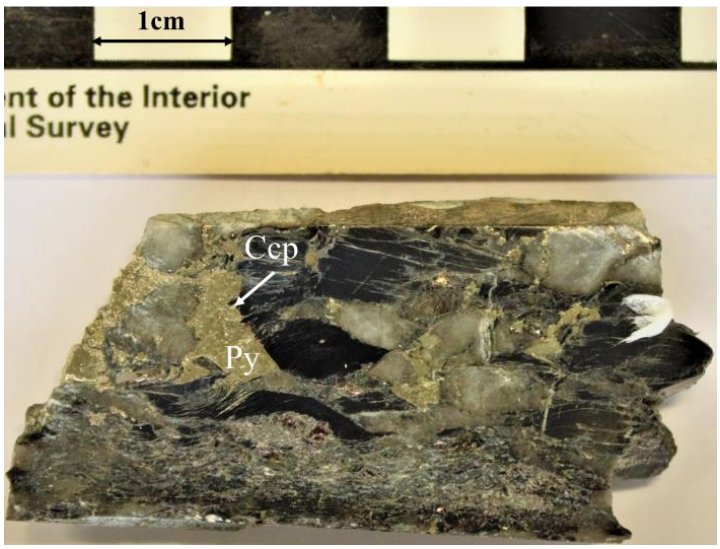

Figure 13. Optical image of the fractured pyrite bearing garnet-quartz-biotite-feldspar gneisses in core PA-1, depth 661.00–661.05 m. Py - pyrite, Ccp – chalcopyrite.

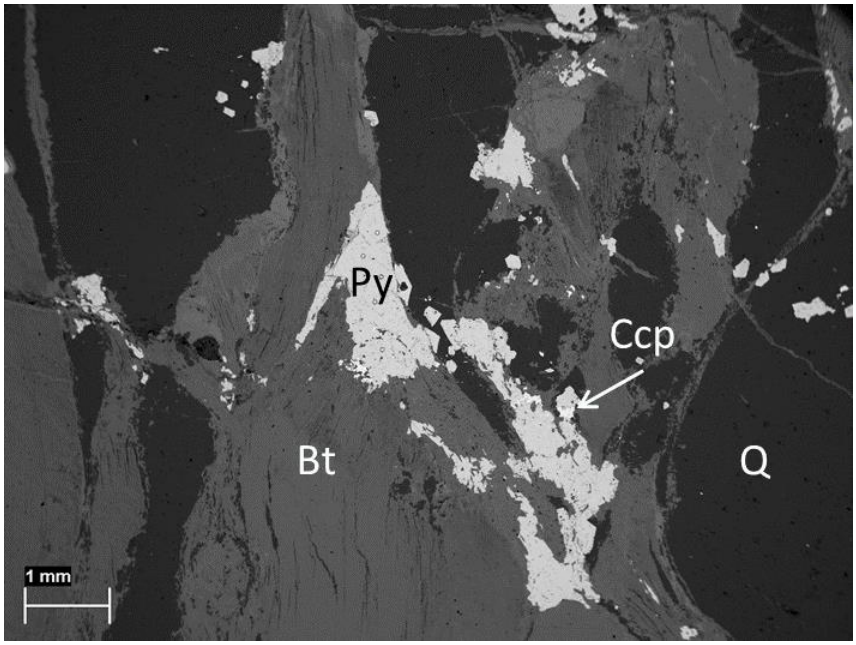

Figure 14. Backscattered scanning electron microscope image of the pyrite (Py) in sample PA1-6s, PA-1 depth 661.00–661.05 m. Py – pyrite, Bt – biotite, Q – quartz, Ccp – chalcopyrite.

Sample PA1-7s (PA-1; 694.30–694.35 m) is from interval where amphibole-magnetite-quartz-garnet gneiss with disseminated pyrite occurs. In this sample the host rock is cut by several

mm-scale intersecting pyrite veins and the whole sample is covered with scattered micron size pyrite crystallites (Figure 15).

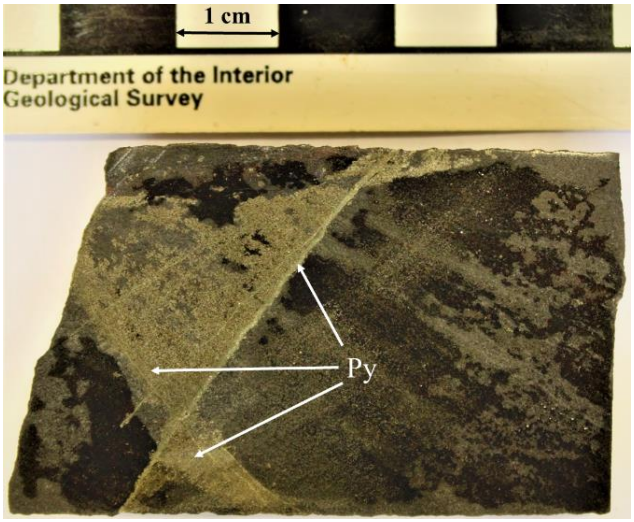

Figure 15. Optical image of the pyrite (Py) veins in drill core PA-1, depth 694.30–694.35 m.

In scanning electron images, the area between undulating pyrite sub-mm veins cross-cutting each other at nearly right angle is in places impregnated with pyrite sub-micrometre aggregates (Figure 16) that seem to replace the quartz and possibly mica so that only garnet has remained in areas impregnated with pyrite (Figure 17).

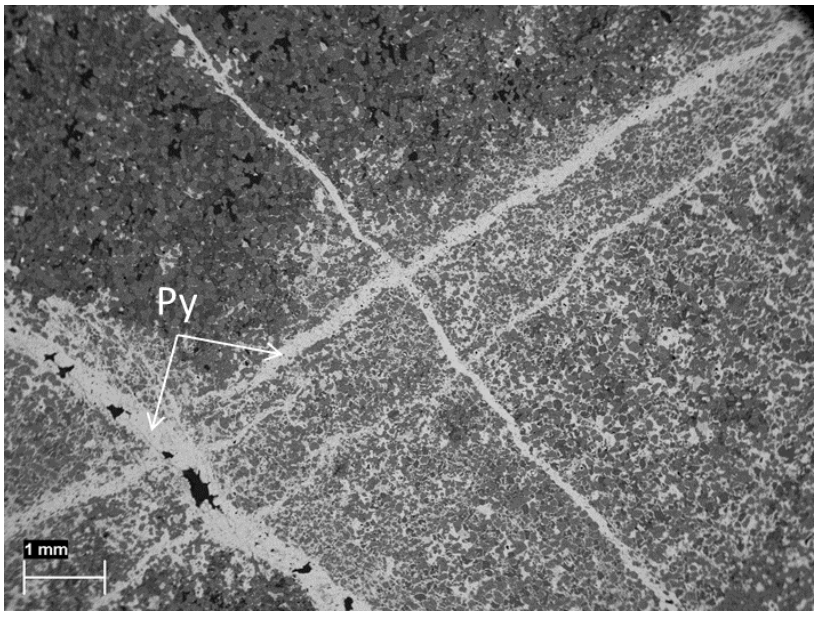

Figure 16. Backscattered scanning electron microscope image of the pyrite (Py) veins and impregnation in sample PA1-7s, drill core PA-1, depth 694.30–694.35 m.

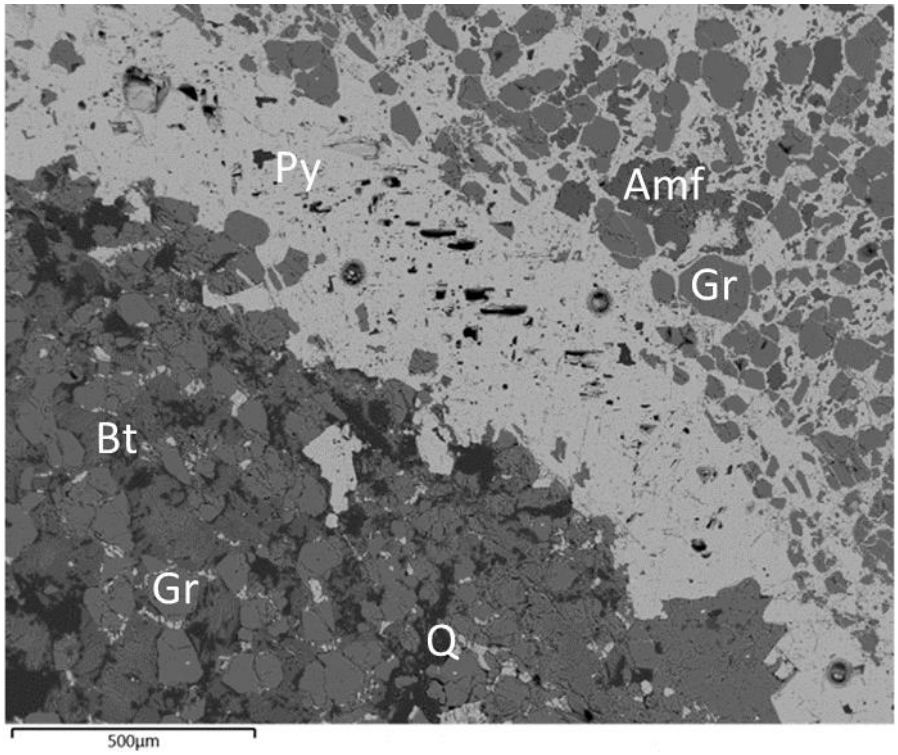

Figure 17. Backscattered scanning electron microscope image of the pyrite (Py) replacing mica and quartz in sample PA1-7s, drill core PA-1, depth 694.30–694.35 m.

Sample PA2-8s (PA-2; 311.50–311.55 m) is from quartz-feldspar-biotite vein in contact with garnet-bearing quartz-biotite-plagioclase gneiss. Sulphides (mainly pyrite) form veinlets of anhedral micrometre scale aggregates protruding the quartz and feldspar host rock (Figure 18).

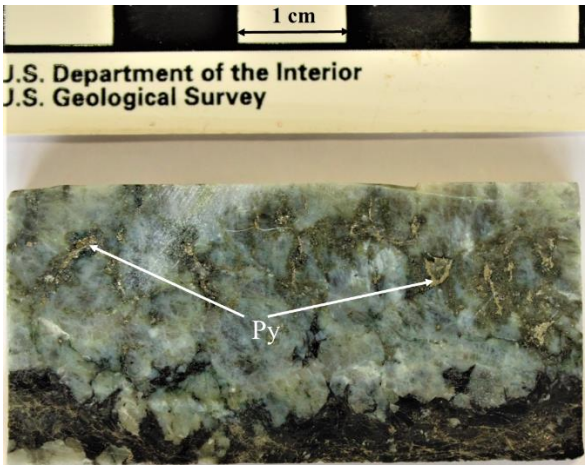

Figure 18. Optical image of the pyrite (Py) inclusions in quartz-feldspar-biotite vein. PA-2 drill core, depth 311.50–311.55 m.

Sample PA2-10s (PA-2; 497.75–497.80 m) is sampled in pyrrhotite bearing garnet-magnetite-pyroxene-quartz gneiss interval. Pyrrhotite (Po) is the dominant sulphide but also pyrite (Py)

and chalcopyrite are present. The pyrrhotite aggregates are typically anhedral to subhedral and reach in size 0.5–1 cm (Figure 19A). In scanning electron microscope the pyrrhotite shows variable composition in backscattered electron image that is mostly controlled by trace elements (Mn, Co) and these areas show distinctively presence of oxygen suggesting that some oxidation has taken place (Figure 19B). Also, anhedral massive pyrrhotite aggregates frequently contain micrometre-size euhedral pyrrhotite crystals.

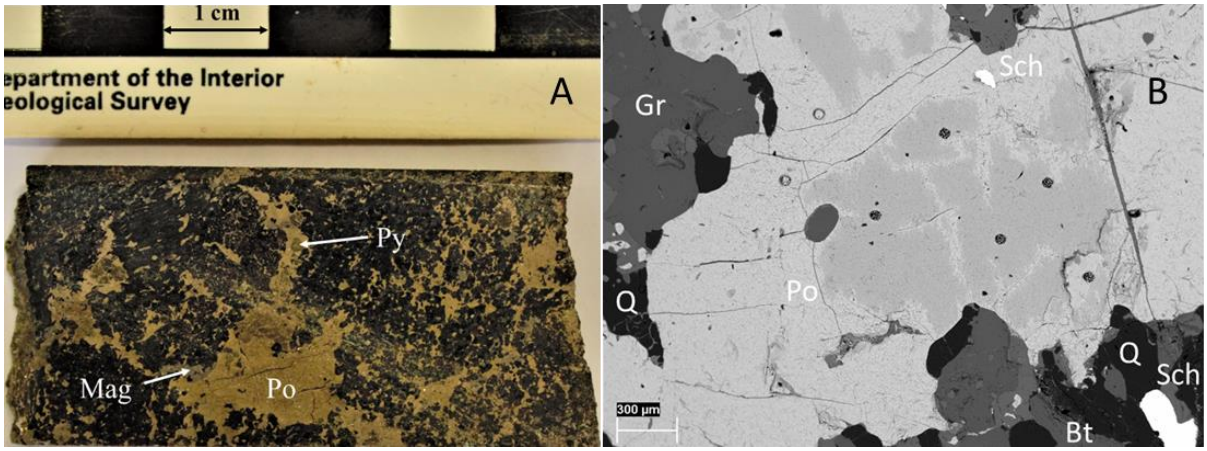

Figure 19. Optical image (A) of the pyrrhotite (Po) massive aggregates and backscattered scanning electron microscope image (B) of the pyrrhotite (Po) anhedral aggregate with varying Fe/S and trace-element content in PA-2, depth 497.75-497.80 m. The darker areas (B) are slightly oxidised. Q - quartz, Gr – garnet, Sch - scheelite, Bt – biotite. Note the laser ablation spots in Po.

Samples PA2-SEM7 (PA-2; 516.30–516.35 m) and TS-00037 (PA-2; 565.00–565.05 m), respectively are from pyrrhotite bearing quartz-biotite-garnet gneiss rocks. In PA2-SEM7 pyrite and pyrrhotite occurs as irregular band/stripes crosscutting the general gneiss banding but sample TS-00037 represents massive-blocky magnetite-sulphide mineralisation of the JMA (Figure 20B).

Figure 20. Optical images of sulphide mineralisation in PA-2 samples PA2-SEM7 (A, 516.30–516.35 m) and TS-00037 (B, 565.00–565.05 m). Po – pyrrhotite, Py – pyrite.

Sample PA2-11s (PA-2; 593.30–593.35 m) is from pyrrhotite bearing-garnet-pyroxene-quartz-magnetite gneiss where abundant magnetite and in places massive-blocky pyrrhotite co-occur with macroscopically visible pyrite and chalcopyrite (Figure 21A).

Samples PA2-SEM8 (PA-2; 629.00–629.05 m) and PA2-12s (PA-2; 712.30–712.35) m are representative of pyrite bearing biotite-amphibole-quartz-magnetite gneiss rock. In former anhedral pyrite aggregates occur in magnetite rich bands and the latter pyrite occurs in mm-size veins-veinlets (Figure 21B, C).

Figure 21. Optical images of the sulphide mineralisation PA-2, depth 593.30–593.35 m (A), 629.00–629.05 m (B), and 712.30–712.35 m (C). Po – pyrrhotite, Py – pyrite, Mag – magnetite, Ccp – chalcopyrite.

Pyrrhotite and Pyrite Trace Element Composition

Trace element composition of the pyrrhotite and pyrite in JMA samples shows high variability, and the most abundant trace elements are Co, Ni and As. The Co content ranges in PA-1 samples from 0.50 to 29 057 ppm (Figure 22A) and in PA-2 samples from 0.46 to 32 552 ppm (Figure 22B).

The most Co enriched Fe-sulphides are in PA-1 at depth 661 m and in drill core PA-2 samples at the depth 497.75 m and 593.30 m. The Ni content ranges in PA-1 samples from 1 to 13 216 ppm (Figure 22A) and in PA-2 samples from 2 to 6253 ppm (Figure 22B).

The As content varies from 0.71–5170 ppm in both cores with the overall median value of 18.75 ppm. The Au content in pyrrhotite and pyrite ranges from below the detection limit (< 0.0007 ppm) up to 0.63 ppm (median 0.02 ppm).

Ag content was in the range of 0.09–181 ppm, and Se and Bi content varied between 3–434 and 0.01–292 ppm, respectively. The highest Au and Ag contents in pyrrhotite/pyrite were in PA-1 sulphides at 661 m depth and in PA-2 samples at the 311.5 m depth (Figure 22AB).

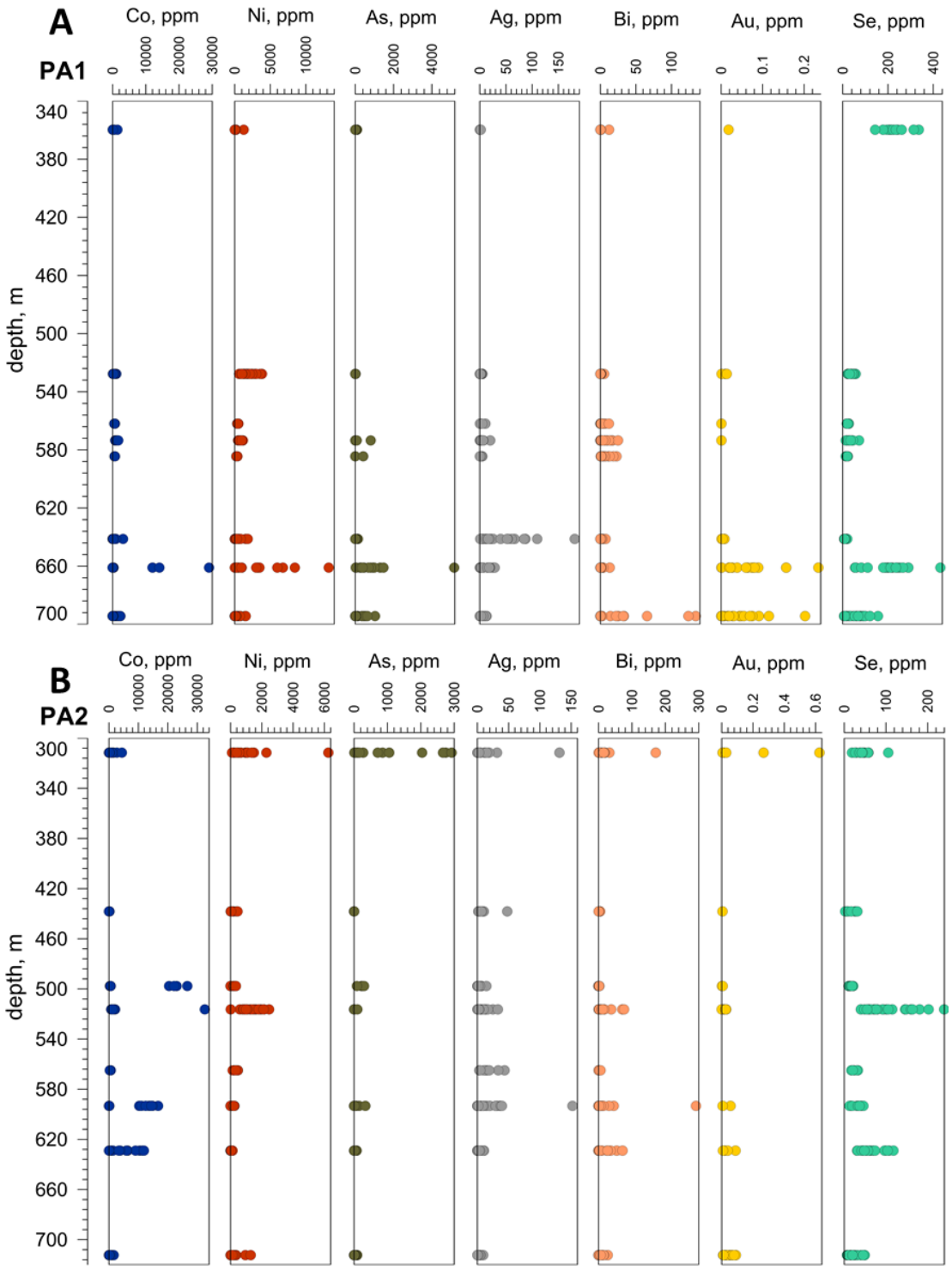

Figure 22. Main trace elements distribution in JMA sulphides. A – PA-1 and B – PA-2

Co and Ni content in different pyrrhotite/pyrite grains in the same sample can be highly variable and often the Co and/or As and Ni content can considerably differ within a crystal aggregate (Figure 23) even if the scanning electron backscattered electron images does not show evidence for zoned crystal growth or different generations.

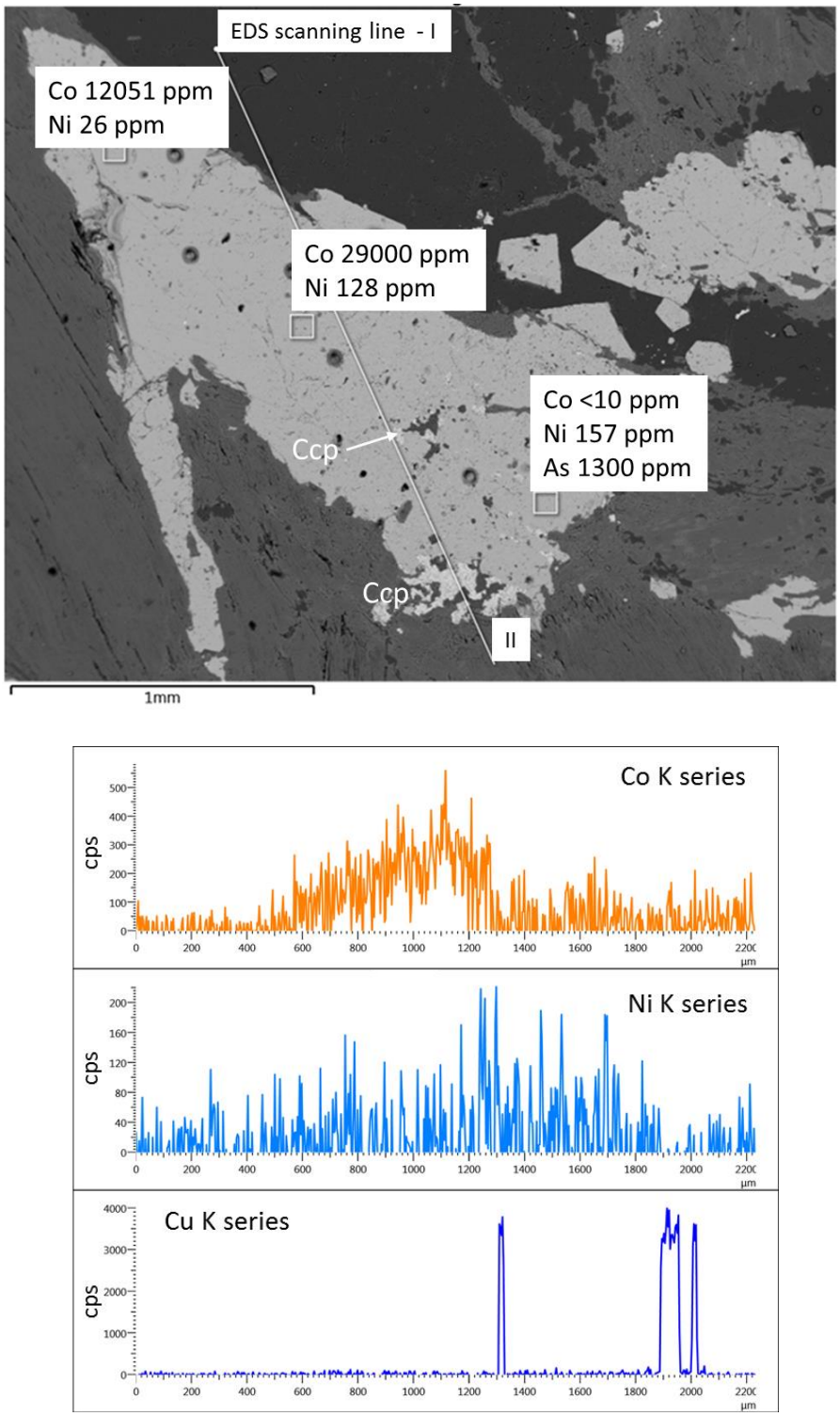

Figure 23. Backscattered SEM image of pyrite aggregate with varying Co and Ni content Element line scans are in counts per second. PA-1, depth 661 m. Ccp – chalcopyrite.

However, in some cases the pyrite inclusions in slightly oxidized pyrrhotite matrix show a clearly different trace element composition (Figure 24).

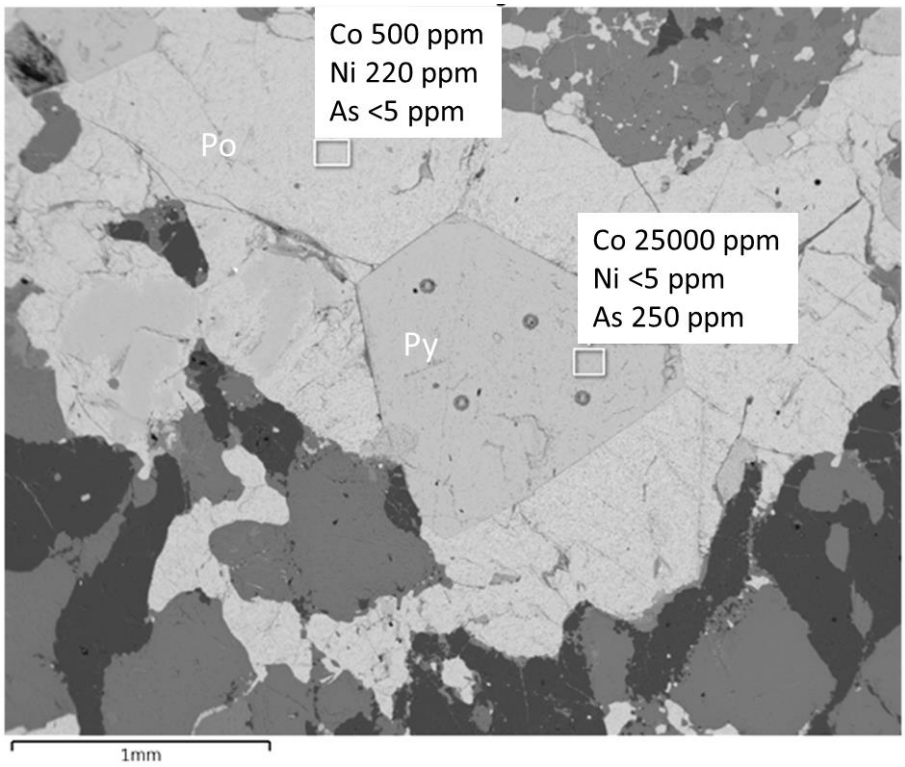

Figure 24. Backscattered SEM image of pyrite crystal in pyrrhotite aggregate with different Co, Ni and As contents. PA-2, depth 497.75 m. Po – pyrrhotite, Py - pyrite.

Discussion

The ratio of Co to Ni in pyrite has been widely used to differentiate geological environments of sulphide formations (Bralia et al., 1979; Bajwah et al., 1987). Bajwah et al. (1987) and Large et al. (2009) have suggested that diagenetic pyrite has Co/Ni ratio ≤2 and hydrothermal pyrite Co/Ni ratio tend to trend away from 1 line. Pyrite and pyrrhotite Co/Ni ratios range from < 0.1 to 10 447 ppm with an average of 212 ppm.

In the plot of Co versus Ni (Figure 25) contents for pyrite and pyrrhotite indicates that most of the samples analysed in JMA drill-cores PA-1 and PA-2 plot in the fields of hydrothermal and sedimentary environment. Some samples indicate volcanogenic environment of the formation but there are no samples that would indicate formation in magmatic environment.

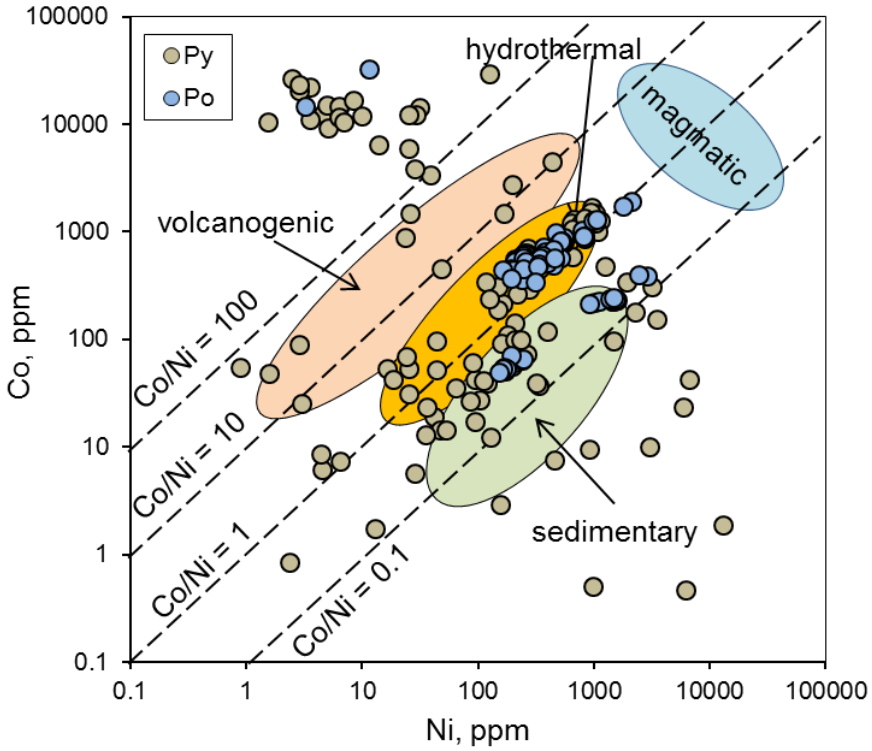

Figure 25. Ni vs. Co plot for pyrite (Py) and pyrrhotite (Po) from JMA drill cores PA-1 and PA-2. Fields for different types of geological environments are from Bralia et al. (1979) and Bajwah et al. (1987).

Samples with the highest Co that plot in the upper left corner do not fit with typical sulphide precipitation geological environments and these analyses may indicate the presence of the Co bearing micro-inclusions within pyrite lattice such as alloclasite [(Co, Fe)AsS] (a member of

the arsenopyrite group) and/or carrollite, ($CuCo_2S_4$), a sulphide of copper and cobalt (Conn et al., 2019). At present the occurrence of such micro-inclusions was not confirmed in SEM study and would require a specific study.

Also, the Ni can be expelled from pyrite during metamorphism and as Ni migrates more easily than Co during metamorphism causing partitioning of Co and Ni between pyrite and pyrrhotite (Conn et al., 2019) leading to the relatively high Co/Ni ratios in pyrrhotite. Therefore, using the Co/Ni ratios of pyrite as an indicator of ore-forming settings where pyrite and pyrrhotite occur in the same deposit has to be taken with caution. However, the high Co values are mostly measured in pyrite grains and only in a few pyrrhotites (Figure 26) which does not support the Co/Ni redistribution hypothesis in pyrite and pyrrhotite in JMA sulphides during metamorphism. Moreover, if the metamorphism has caused the preferential Ni mobilisation, then this effect must have influenced the whole section, but the Co/Ni ratios show a large variability between different adjacent samples and within the same sample (Figure 23).

The samples with high Co/Ni ratio are found in both drillcores PA-1 and PA-2 at depths 661.05; 497.75, 593.3 and 629, respectively. These samples with the high Co/Ni ratio do not differ from other samples by rock type and petrography expect high Co content. Almost all samples with the high Co content are from pyrite, only few samples are from pyrrhotite.

Pettai (2021) studied the fracturing of the rocks in JMA drill cores PA-1 and PA-2, and distinguished fractures with carbonate infill, sulphide infill, carbonate and sulphide infill, and also clean fractures (slickensides). This study showed that on the basis of the most common directions of dip angles, the sulphide-filled fractures form a different system from carbonate-filled and unfilled fracture systems. The most Co enriched sulphides are found in drill-core PA-2 at depths 497 and 593 m. These samples are from intervals characterised by sulphide filled fractures, and sulphide-carbonate and carbonate filled fractures, respectively. Similar fracture/vein types are found in other interval and neither the orientation nor dip angle differ from other similar fractures measured in the both drill cores (Table 1).

Table 1. Samples with the highest Co content and the orientation of the fractures in the same interval. Fracture types - FCA - Fractures with carbonate infill; FSU - Fractures with sulphide infill, FCS - Fractures with, carbonate and sulphide infill, FCL - Clean fractures (slickenside)

Sample	Depth, m	Dip	Azimuth	Type	Co, ppm
PA1-6s	661.05	54.071	76.855	FCA	29 000 – 12 000
PA2-8s	311.53	44.393	169.426	FCA	4400 – 2700
PA2-10s	497.89	5.31	39.446	FSU	26 500-20 400
PA2-10s	497.17	4.66	27.486	FSU	26 500-20 400
PA2-11s	593.97	18.761	31.14	FCS	16 700-10 280
PA2-11s	593.04	0.431	298.718	FCA	16 700-10 280
PA2-11s	593.52	75.326	166.789	FCA	16 700-10 280
PA2-SEM8	629.57	80.003	110.717	FCA	11 900 - 2700
PA2-SEM8	629.39	80.105	182.702	FCL	11 900 - 2700

Maslennikov et al. (2009) showed that elevated Se content in pyrite/pyrrhotite (30-300 ppm Se) can be used for inferring high-temperature deposition (*ca*. 250–350 °C), and Tl content for inferring pyrite low-temperature deposition (*ca*. 100–250 °C). By their study a Se/Tl ratio of 10 separates the low- and high-temperature fields.

According to Se/Tl ratio most of the analysed sulphides in JMA drill cores PA-1 and PA-2 plot below the Se/Tl ratio 10 indicating formation in high-temperature conditions, and only a few analysed values plot on the line or above (Figure 26).

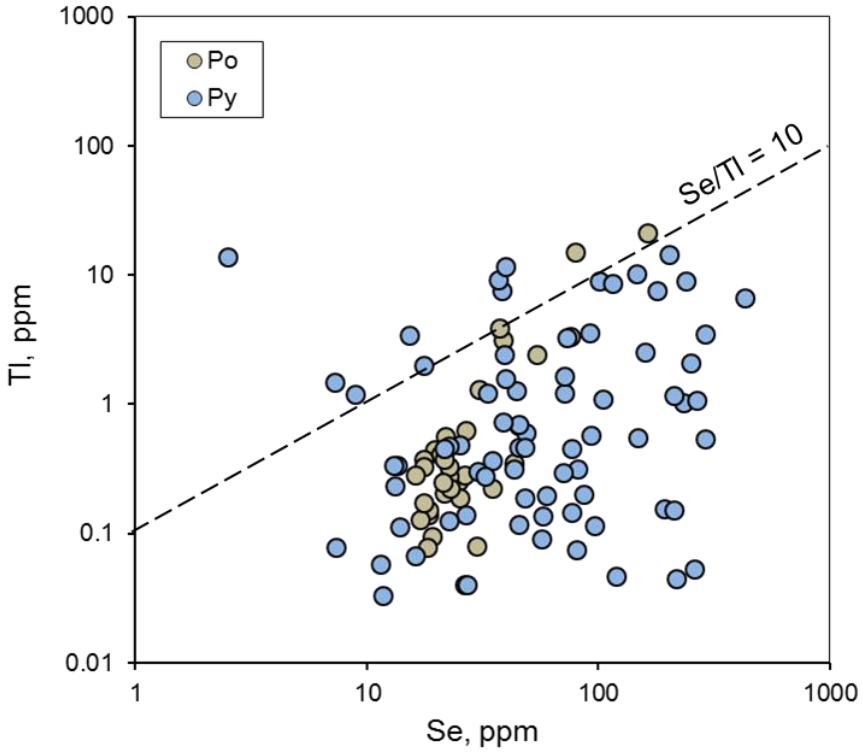

Figure 26. Se vs. Tl cross-plot for sulphides in JMA drill cores PA-1 and PA-2. The Se/Tl ratio of 10 denotes the low temperature (100–250 °C) field above the line and the high-temperature (250–350 °C) field below (Maslennikov et al., 2009).

On As vs Au content in sulphides plot most of the analysed points in JMA sulphides plot outside the hydrothermal and diagenetic pyrite fields defined by Large et al. (2009) for gold-bearing deposits (Figure 27). However, analyses plotting at the boundary or in the hydrothermal-diagenetic fields show slight covariation between gold and arsenic as seen in many gold deposits worldwide (Large et al., 2009). Also, as typical for both diagenetic and hydrothermal pyrites, all analysed sulphides plot well below the gold saturation line for arsenic bearing pyrite (Large et al., 2009). This suggests that Au in analysed pyrrhotite and pyrite occurs as a solid solution in the sulphide crystal structure, not in a form of native Au inclusions.

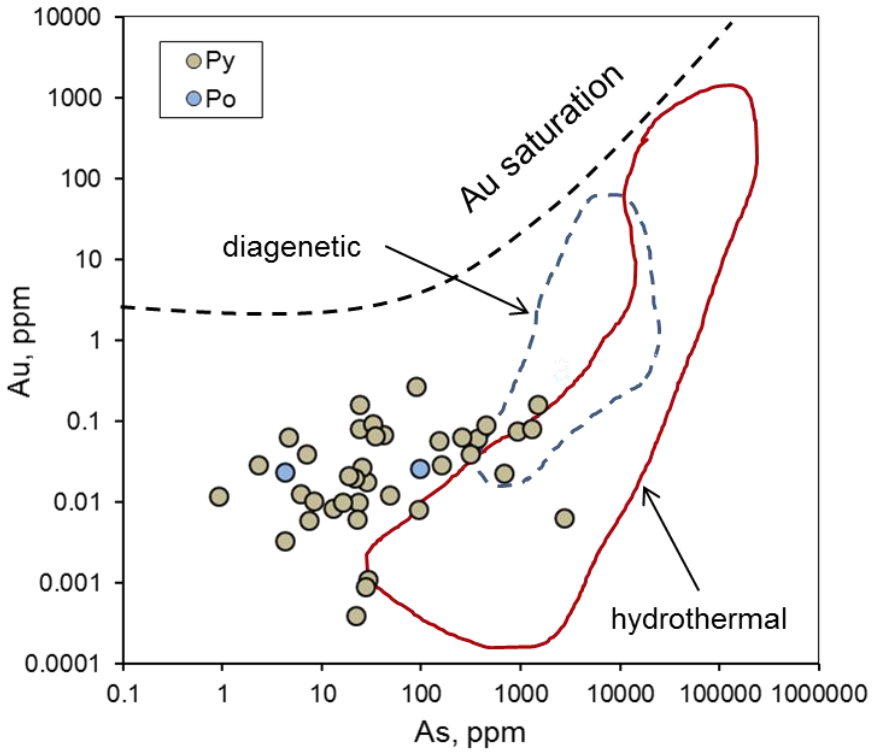

Figure 27. As versus Au variation in pyrite and pyrrhotite in JMA drill cores PA-1 and PA-2. The Au saturation line and fields from hydrothermal and diagenetic pyrites is from Large et al., (2009).

In contrast in the As-Te plot (Figure 28) some of the analyses are at or above the Te solubility line indicating that some of Te might be present in sulphides as telluride inclusions. This is because the substitution of Te^{2-} for S^{2-} is restricted in sulphides compared to Se^{2-} due to differences in ionic radius, and because of that Te commonly forms its own minerals (tellurides, sulphotellurides, and sulphosalts) in hydrothermal conditions (e.g., Ciobanu et al., 2006). Indeed, native Te and Te-Bi, and Te-Ag intermetallic compounds are found in JMA intervals with sulphide mineralisation (Figure 29).

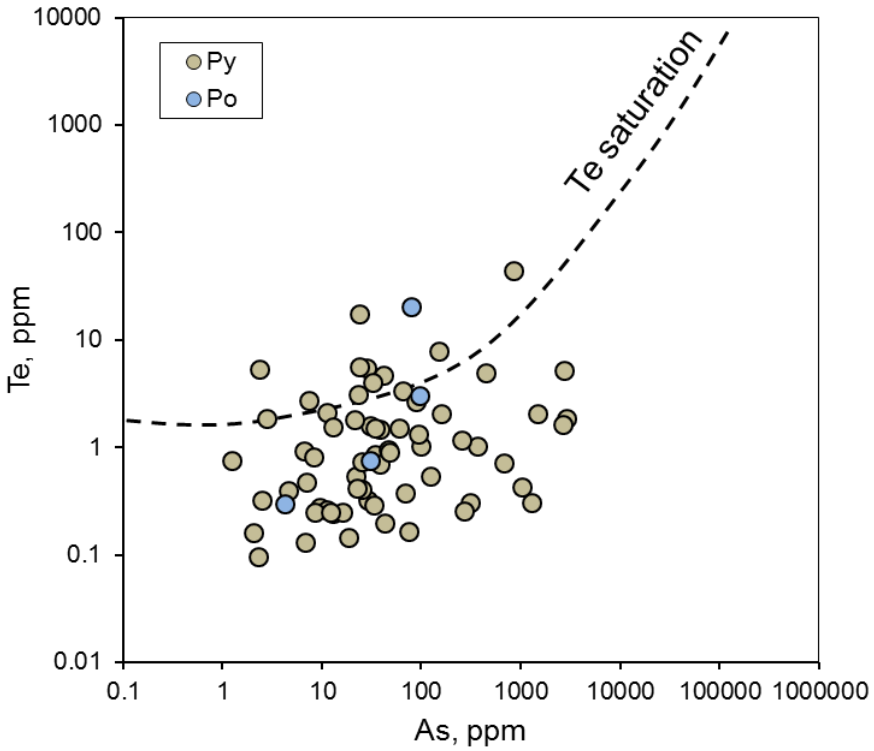

Figure 28. As versus Te plot in pyrite and pyrrhotite in JMA drill cores PA1 and PA2. The solubility limit for Te in pyrite is from Keith et al., (2020).

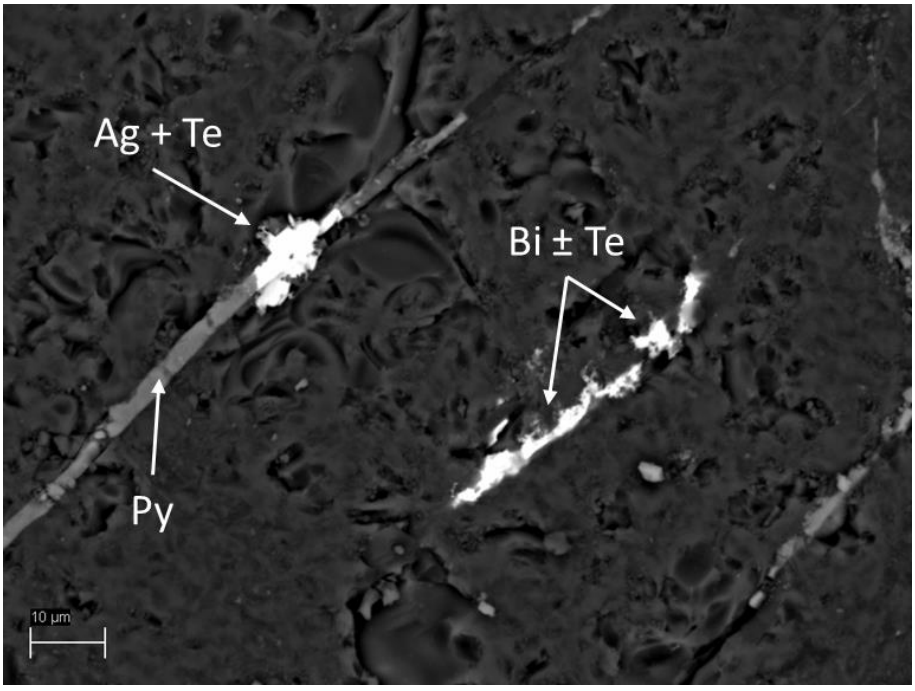

Figure 29. Native Te, Ag and Bi drill core PA-1, depth 562 m.

The principal component analysis (PCA) of the trace elements present in most of the analysed sulphides (Co, Ni, Bi, Pb, Cu and Se) shows that 60% cumulative variance is described by the first two principal components and first three components describe 73% of the variance (Table 2; Figure 30).

Table 2. Standard deviation and importance of principal components for the trace elements Co, Ni, Bi, Pb, Cu and Se in pyrite and pyrrhotite.

	Comp.1	Comp.2	Comp.3	Comp.4	Comp.5	Comp.6
Standard deviation	1.51	1.15	0.87	0.81	0.74	0.64
Proportion of Variance	0.38	0.22	0.13	0.11	0.09	0.07
Cumulative Proportion	0.38	0.60	0.73	0.84	0.93	1.00

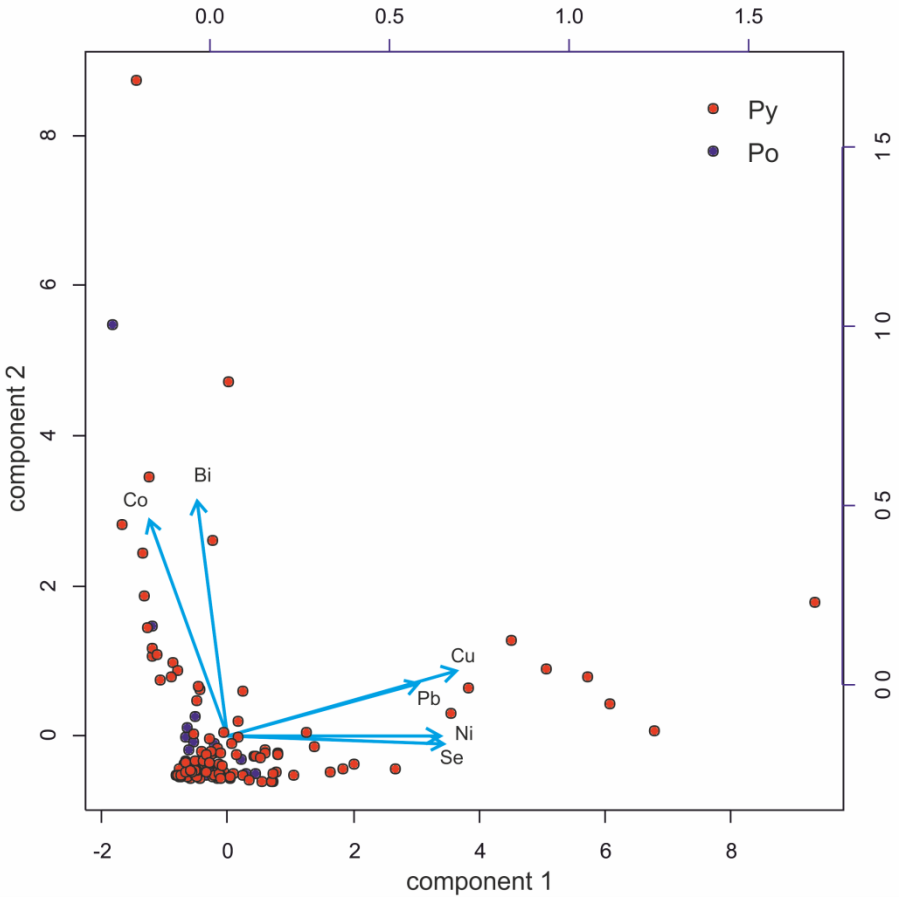

Figure 30. Principal components 1 and 2 plotted for Co, Ni, Bi, Pb, Cu and Se in pyrite and pyrrhotite.

The first principal component describes 38% of the variance and correlates with increased content of Ni, Co, Pb and Se (Table 3). The second principal component describes 22% of the

variance and correlates strongly with an increase in Co and Bi. The third principal component accounts for only 13% of the variance and correlates with decreasing Ni but also increasing Pb and Se (Table 3).

Table 3. Correlation matrix for four first principal components for the trace elements Co, Ni, Bi, Pb, Cu and Se in pyrite and pyrrhotite

	Comp.1	Comp.2	Comp.3	Comp.4
Co	-0.147	0.676	0.128	0.683
Ni	0.486	0.000	-0.616	0.172
Cu	0.548	0.154	-0.271	0.003
Se	0.488	0.011	0.396	0.226
Pb	0.449	0.102	0.591	-0.279
Bi	-0.050	0.713	-0.154	-0.612

This data shows that the analysed dataset includes three different groups – the majority of sulphides show moderate trace element content and two separate groups with high Co and Bi, and sulphides enriched with Ni, Cu, Se and Pb. Steadman et al. (2021) and Maslennikov et al. (2009) proposed that trace element associations can be used to estimate their formation temperatures. High-temperature group (>300 °C) should be characterised by elevated Co, Ni, Cu, Se, Te and Bi whereas the mid-temperature group (200–300 °C) and low-temperature group (150–200 °C) are characterised by Zn-As-Sb-Sn, and Pb-Sb-Ag-Bi-Au-Tl-Mn associations.

By this, both groups in JMA sulphides that differ from the rest of the pyrite/pyrrhotite samples by high Co, Bi, Ni, Se and Cu are indicative of the high-temperature conditions but probably with different fluid composition. Further research should be pointed into revealing the unusually high Co enrichment in some of the analysed sulphides and its relationships to the potential mineralising fluids.

It is interesting that if principal components analysis is applied for Co, Ni, Bi, Pb, Cu, Se, As, Ag and Au system where only one pyrrhotite sample remains in data set then these two groups defined by Co-Bi and Ni-Se-Cu-Pb, respectively do not show clear covariance with Ag or Au, which are correlated with the As (particularly strongly with Ag) content in pyrite (Figure 31).

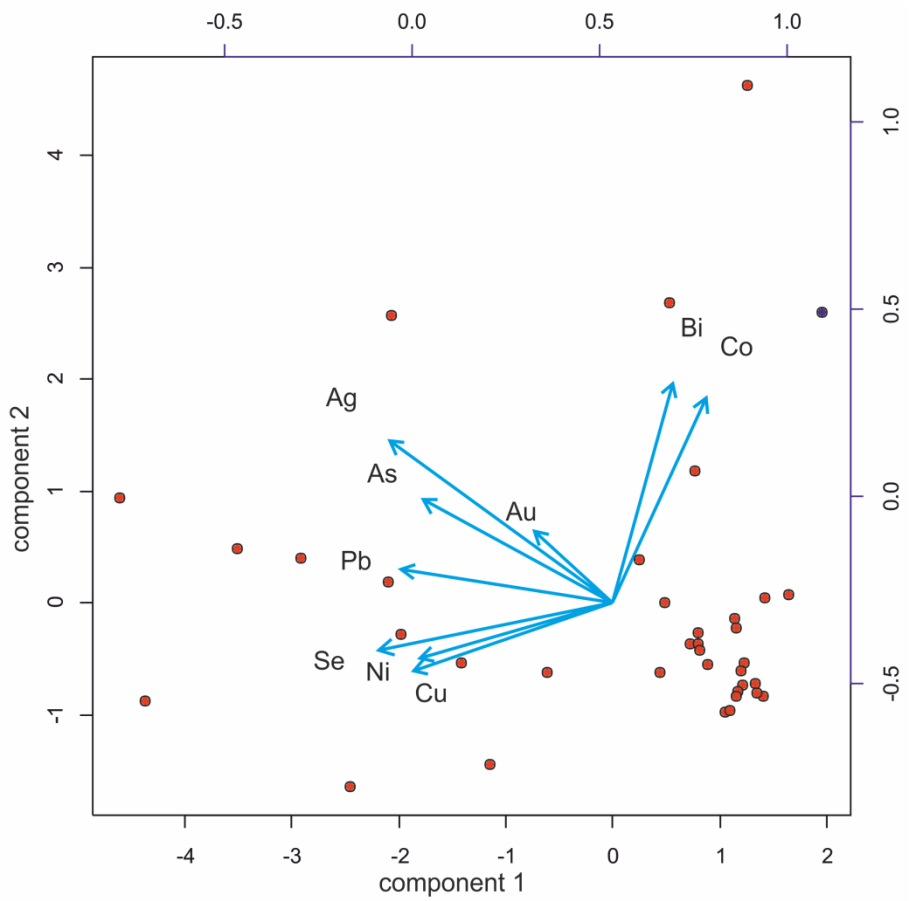

Figure 31. Principal components 1 and 2 plotted for Co, Ni, Bi, Pb, Cu, Se, As, Ag and Au in pyrite and pyrrhotite.

It has been shown that As substitution to S in pyrite structure causes structural defects because of the differences in ionic radii and introduces charge imbalance as As is monovalent (As^{-}) and sulphur is in pyrite divalent (S^{2-}) (Large and Maslennikov, 2020). Therefore As substitution helps other ions to introduce to pyrite structure and earlier studies have pointed out positive covariation between As and other typically large ion-radius elements like Au, Ag, Cd, Pb, Tl and Sb (Keith et al., 2018; George et al. 2019).

Summary

This thesis investigated in 2019 drilled western Jõhvi magnetic anomaly core PA-1 and PA-2 sulphide intervals where pyrite and pyrrhotite occurs. For this purpose, 15 samples from intervals of sulphide mineralisation were characterised and analysed, of which 13 were slabs and 2 were thin sections. The petrography of the samples was described and the trace elements present in them were determined, which allowed their formation conditions to be characterised. The mineralogy of the samples was analysed by scanning electron microscopy (SEM) and the presence of trace elements by laser ablation inductively coupled plasma mass spectrometry (LA-ICP-MS). The main trace elements used were Co, Ni and As, but also Au, Ag, Bi and Se, which were present in almost all 246 samples analysed, of which 145 were pyrite and 99 pyrrhotite.

Iron sulphides pyrite and, pyrrhotite in Jõhvi magnetic anomaly rocks are found throughout the Jõhvi crystalline rock succession as scattered crystal and intensively mineralised zones that frequently co-occur with magnetite mineralisation. The pyrrhotite typically forms irregular-anhedral sulphide masses but pyrite occurs mostly as euhedral-subhedral crystalline aggregates of varying crystallite size from µm to cm-scale. The sulphide mineralisation is often associated with deformed-fractured zones of the rock succession.

Trace element composition (Ni/Co) of pyrites and pyrrhotites show that sulphides are mostly of hydrothermal orging but also a population of sulphides plotting on typical sedimentary field is present. Some analyses indicate volcanogenic environment of the formation but there are no samples that would indicate formation in magmatic environment. There is a number of samples that show significant Co enrichment (>20 000 ppm) which is possibly due to Co-mineral microinclusions but further study is needed to decipher the nature of the Co enrichment.

The Se and Tl ratio of the analysed pyrites and pyrrhotites suggests that major part of samples are of high-temperature (250–350 °C) origin and only few samples suggest low-temperature (100–250 °C) origin. Also, the Au vs As plot suggested that Au occurs as a solid solution in the sulphide crystal structure, not in a form of native Au inclusions while Te and Te-Bi, and Te-Ag intermetallic compounds are found in JMA intervals with sulphide mineralisation.

Principal component analysis of the sulphide trace element compositions showed three groups: main sequence with low-to-moderate trace-element enrichments, Co-Bi rich association and Ni-Se-Cu-Pb association. Two last associations are both indicative of high-temperature

hydrothermal fluids with probably a different composition and possibly different timing that needs to be proven by a further study.

Kokkuvõte

Käesolevas töös uuriti 2019. aastal Jõhvi läänepoolseimasse magnetanomaaliasse puuritud puursüdamikes PA-1 ja PA-2 sulfiidistunud intervalle, kus esines püriiti ja pürrotiini. Selleks kirjeldati ja analüüsiti 15 proovi, millest 13 olid lihvid ja 2 õhikud. Kirjeldati proovide petrograafiat ja määrati neis esinevaid jälgelemente, mille põhjal iseloomustati nende tekketingimusi. Proovide mineraloogilist koostist analüüsiti skaneeriva elektronmikroskoobiga (SEM) ja jälgelementide esinemist laser-ablatsiooni induktiivsidestatud plasma massispektromeeriga (LA-ICP-MS). Põhiliste jälgelementidena kasutati edasises analüüsis Co, Ni ja As, aga ka Au, Ag, Bi ja Se sisaldusi 246 analüüsipunktist, millest 145 esindavad püriiti ja 99 pürrotiini.

Co/Ni suhte alusel jagunesid proovid kahte põhilisse tekkegruppi: hüdrotermaalsed ja settelised. Üksikud proovid näitasid vulkanogeenset tekketingimust ja ühtegi analüüsi ei kvalifitseerunud magmalise tekketingimuse alla. Samuti eristusid eriti kõrgete Co sisaldustega sulfiidid, mis teistest sulfiididest kivimtüübi petrograafilise kirjelduse alusel selgelt ei eristunud. Co rikkad sulfiidid oli tüüpiliselt purstatud-lõhelistes kivimites, aga seost kindlat lõhetüübi ja selle täitega ei eristunud, mistõttu vajab see küsimus veel põhjalikumat uurimist. Võib oletada, et kõrged Co sisaldused seotud on sulfiidides olevate Co-mineraalide mikrosuletistega.

Se ja Tl sisalduste järgi on analüüsitud sulfiidid moodustunud kõrgetemperatuurilistes hüdtotermaalsetes tingimustes (250–350 °C). Jälgelementide koosluste põhikomponentide analüüsi põhjal jagunevad analüüsitud sulfiidid kolme gruppi: põhipopulatsioon, kus jälgelementide sisaldused on madalad ja või keskmised; Co ja Bi rikkad ning Ni, Cu, Se, Pb rikkad sulfiidid. Kõrgemad elementide sisaldused tulevad esile peamiselt püriidis, üksikute eranditena on kõik pürrotiinid põhirühmas. Kaks eristuvat assotsiatsiooni on mõlemad arvatavasti kõrge-temperatuurilised hüdrotermaalsed, aga esindavad erineva koostisega fluide ning on arvatavasti erineva tekkeajaga.

Acknowledgements

The author would like to express the gratitude to supervisors Kalle Kirsimäe and Siim Nirgi for helping with every aspect. Also Marian Külaviir for assistance with the scanning electron microscope (SEM) and Päärn Paiste for his assistance in the use of inductively coupled plasma mass spectrometry (ICP-MS).

References

Bajwah, Z., Seccombe, P., Offler, R., 1987. Trace element distribution, Co/Ni ratios and genesis of the Big Cadia iron-copper deposit, New South Wales, Australia. Mineralium Deposita, 22, 292–300.

Bogdanova S., Gorbachev R., Skridlaite G., Soesoo A., Taran L., Kurlovich D., 2015. Trans-Baltic Palaeoproterozoic correlations towards the reconstruction of supercontinent Columbia/Nuna. Precambrian Research, 259, 5–33.

Bralia, A., Sabatini, G., Troja, F., 1979. A revaluation of the Co/Ni ratio in pyrite as geochemical tool in ore genesis problems. Mineralium Deposita, 14, 353–374.

Ciobanu, C. L., Cook, N. J., Spry, P. G., 2006. Preface – Special Issue: Telluride and selenide minerals in gold deposits – how and why?. Mineralogy and Petrology, 87 (3). 163-169.

Conn, C. D., Spry, P. G., Layton-Matthews, D., Voinot, A., Koenig, A., 2019. The effects of amphibolite facies metamorphism on the trace element composition of pyrite and pyrrhotite in the Cambrian Nairne Pyrite Member, Kanmantoo Group, South Australia. Ore Geology Reviews, 114, 103128.

Cook, N., Chryssoulis, S., 1990. Concentrations of invisible gold in the common sulfides. The Canadian Mineralogist, 28, 1–16.

Deditius, A. P., Reich, M., 2016. Constraints on the solid solubility of Hg, Tl, and Cd in arsenian pyrite. American Mineralogist, 101, 1451–1459.

Duran, C. J., Barnes, S. J., Corkery, J. T., 2015. Chalcophile and platinum-group element distribution in pyrites from the sulfide-rich pods of the Lac des Iles Pd deposits, Western Ontario, Canada: Implications for post-cumulus re-equilibration of the ore and the use of pyrite compositions in exploration, Journal of Geochemical Exploration., 158, 223–242

Erisalu E., Arvisto E., 1969. Report of the basement studies on Jõhvi magnetic anomaly and nearby. Tallinn: Geological Survey of Estonia, EGF 3032, 1–257. [In Russian]

George, L. L., Biagioni, C., D'Orazio, M., Cook, N. J., 2018. Textural and trace element evolution of pyrite during greenschist facies metamorphic recrystallization in the southern Apuan Alps (Tuscany, Italy): Influence on the formation of Tl-rich sulfosalt melt, Ore Geology Reviews, 102, 59–105.

Keith, M., Haase, K., Klemd, R., Smith, D., Schwarz-Schampera, U., Bach, W., 2018. Constraints on the source of Cu in a submarine magmatic-hydrothermal system, Brothers volcano, Kermadec island arc. Contributions to Mineralogy and Petrology, 173.

Keith, M., Smith, D., Doyle, K., Holwell, D., Jenkin, G., Barry, T., Becker, J., Rampe, J., 2020. Pyrite chemistry: A new window into Au-Te ore-forming processes in alkaline epithermal districts, Cripple Creek, Colorado. Geochimica et Cosmochimica Acta.

Koppelmaa. H., 2002 Estonian crystalline basement geological mapping. Scale 1:400 000. Headnote.

Large, R.R., Danyushevsky, L., Hollit, C., Maslennikov, V., Meffre, S., Gilbert, S., Bull, S., Scott, R., Emsbo, P., Thomas, H., Singh, B., Foster, J., 2009. Gold and trace element zonation in pyrite using a laser imaging technique: implications for the timing of gold in orogenic and Carlin-style sediment-hosted deposits. Economic Geololgy. 104, 635–668.

Linari, A.A., 1940. Report on diamond drilling near Jõhvi. Editions of Tallinn University of Technology, 15, 1–27.

Luha, A., 1946. Earth Resources in the USSR. Concluding Overview of Geological Appliances. Teaduslik Kirjandus, Tartu, 1–176. [In Estonian]

Mathieu, L., 2019. Detecting magmatic-derived fluids using pyrite chemistry: Example of the Chibougamau area, Abitibi Subprovince. Québec. Ore Geology Reviews, Volume 114, 103127, ISSN 0169-1368.

Maslennikov, V.V., Maslennikova, S.P., Large, R.R.,Danyushevsky, L.V., 2009. Study of trace element zonation in vent chimneys from the Silurian Yaman-Kasy volcanic-hosted massive sulfide deposit (Southern Urals, Russia) using laser ablation-inductively coupled plasma mass spectrometry (LA-ICPMS). Economic Geology,104, 1111–1141.

Nirgi, S., Maala, L., Kaasik, T., Smyth, D., Wrobel, F., 2022. Assessment of the Exploration Potential of the Jõhvi Magnetic Anomaly, NE Estonia.

Nirgi, S., Soesoo, A., 2021. Geology and Geochemistry of a Paleoproterozoic Iron Mineralization in North-Eastern Estonia. Proceedings of the Karelian Research Centre of the Russian Academy of Sciences, 25.

Pettai, K., 2021. Structural analysis of the crystalline rocks at the Jõhvi magnetic anomaly. University of Tartu. Geology department. Bachelor’s thesis. 1-59.

Plado, J., Kiik, K., Jokinen, J., Soesoo, A., 2020. Magnetic anomaly of the Jõhvi iron ore, northeastern Estonia, controlled by subvertical remanent magnetization. Estonian Journal of Earth Sciences, 69, 189–199.

Puura, V., Flodèn, T., 1996. Subjotnian igneous structures in the Svecofennian domain of the Baltic region. GFF, 118, Jubilee Issue, 22–23.

Reich M, Deditius A, Chryssoulis S, Li J-W, Ma C-Q, Parada MA, BarraF, Mittermayr F., 2013. Pyrite as a record of hydrothermal fluidevolution in a porphyry copper system: a SIMS/EMPA trace ele-ment study. Geochimica et Cosmochimica Acta 104:42–62.

Soesoo, A., 2004. Precambrian basement of Estonia. Proceedings of the Estonian Acadademy of Science, 53, 3, 147–148.

Soesoo, A., Nirgi, S., Plado, J., 2020. The evolution of the Estonian Precambrian basement: geological, geophysical and geochronological constraints. Proceedings of the Karelian Research Centre of the Russian Academy of Sciences, 10, 18–33.

Soesoo, A., Nirgi, S., Urtson, K., Voolma, M., 2021. Geochemistry, mineral chemistry and pressure– temperature conditions of the Jõhvi magnetite quartzites and magnetite-rich gneisses, NE Estonia. Estonian Journal of Earth Sciences, 70, 2, 71–93.

Soesoo, A., Plado, J., Nirgi, S., 2020. Metallogenesis of magnetic anomaly in NE Estonia. R&D project no. LLTOM17351 (RITA1/01-01-08) Estonian Research Council. EGF:9404. 1–13.

Soesoo, A., Puura, V., Kirs, J., Petersell, V., Niin, M., All, T., 2004. Outlines of the Precambrian basement of Estonia. Proceedings of the Estonian Academy of Sciences. Geology, 53, 3, 149–164.

Steadman, J.A., Large, R.R., Meffre, S., Olin, P.H., Danyushevsky, L.V., Gregory, D.D., Holden, P., 2015. Synsedimentary to early diagenetic gold in black shale-hosted pyrite nodules at the Golden Mile Deposit, Kalgoorlie, Western Australia. Economic Geology. 110, 1157–1191.

Steadman, J.A., Large, R., Olin, P.H., Danyushevsky, L., Meffre, S., Huston, D.L., Fabris, A., Lisitsin, V., Wells, T., 2020. Pyrite trace element behavior in magmatic-hydrothermal environments: An LA-ICPMS imaging study. Ore Geology Reviews, 103878.

Suuroja, K., 1969. Jõhvi magnetiitse maagistumise iseloomust. Tartu Ülikool, Geoloogia kateeder. Diplomitöö, 1–88.

Sykora, S., Selley, D., Cooke, Harris, A.C., 2018. The Structure and Significance of Anhydrite-Bearing Vein Arrays, Lienetz Orebody, Lihir Gold Deposit, Papua New Guinea. Economic Geology, 113, 237-270.

Vaher, R., Puura, V., Erisalu, E., 1962. The tectonic pattern of Northeast Estonia. ENSV TA Geoloogia Instituudi Uurimused, 319–335, https://www.etera.ee/s/odBf1Ev3SG. [In Russian]

Internet references

Geological base map 1:400 000. https://geoportaal.maaamet.ee/est/Ruumiandmed/Geoloogilisedandmed/Geoloogilised-kaardid-1-400000-p356.html (Last viewed 02.05.2022)

Tartu Ülikooli loodus- ja täppisteaduste valdkonna õppeprodekaanile

Taotlus lõputöö avaldamisele piirangute kehtestamiseks ja lõputöö kaitsmise kinniseks kuulutamiseks

Nimi	Alvar Ratt
Sünniaeg	30.01.1998
Õppekava	Geoloogia ja keskkonnatehnoloogia
Juhendaja	Kalle Kirsimäe ja Siim Nirgi
Lõputöö pealkiri	Pyrrhotite and pyrite trace element composition in Jõhvi magnetite quartzites, north-east Estonia: implications to sulphide mineralisation processes

[X] Palun **mitte avaldada** minu lõputööd kuni **27.05.2023**

- [ ] teistele isikutele kuuluvate varaliste autoriõiguste tõttu.
- [ ] kuna töö sisaldab isikuandmeid, mille avaldamiseks pole andmesubjekti nõusolekut.
- [ ] riigisaladuse tõttu.
- [ ] ärisaladuse tõttu.
- [X] lõputöö avaldatakse tulevikus teadusartiklina.
- [ ] muul põhjusel.

Selgitus (*põhjendus, miks taotletakse piiranguid ja miks just selliseks perioodiks*):

[ ] Palun kuulutada minu **lõputöö kaitsmine kinniseks.**

Selgitus (*põhjendus, miks taotletakse lõputöö kaitsmise kinniseks kuulutamist*):

Taotlusele on lisatud järgmised lisad (*täita juhul, kui taotlusel on lisad, nt äriühingu poolne kinnitus, et töö sisaldab ärisaladust)*:

1.
2.

Kuupäev ja üliõpilase allkiri: 27.05.2022 Alvar Ratt

Kuupäev ja juhendaja allkiri: 27.05.2022 Siim Nirgi